Development, intercomparison and evaluation of an improved mechanism for the oxidation of dimethyl sulfide in the UKCA model

Ben A. Cala[1,*], Scott Archer-Nicholls[1,#], James Weber[1,$], N. Luke Abraham[1,2], Paul T. Griffiths[1,2], Lorrie Jacob[1], Y. Matthew Shin[1], Laura E. Revell[3], Matthew Woodhouse[4], Alexander T. Archibald[1,2]

[1]Yusuf Hamied Department of Chemistry, University of Cambridge, Cambridge, CB2 1EW, UK
[2]National Centre for Atmospheric Science, Cambridge, CB2 1EW, UK.
[3]School of Physical and Chemical Sciences, University of Canterbury, Christchurch, New Zealand.
[4]CSIRO Oceans and Atmosphere, Aspendale, 3195, Australia.
*Now at Department of Ocean Systems (OCS), NIOZ Royal Netherlands Institute for Sea Research, Texel, the Netherlands
#Now at IT Services, University of Manchester, Manchester, M13 9PL, UK.
$Now at School of Biosciences, University of Sheffield, S10 2TN, UK.

Correspondence to: Alexander T. Archibald ata27@cam.ac.uk and Ben. A. Cala ben.cala@nioz.nl

Abstract. Dimethyl sulfide (DMS) is an important trace gas emitted from the ocean. The oxidation of DMS has long been recognised as being important for global climate through the role DMS plays in setting the sulfate aerosol background in the troposphere. However, the mechanisms in which DMS is oxidised are very complex and have proved elusive to accurately determine in spite of decades of research. As a result the representation of DMS oxidation in global chemistry-climate models is often greatly simplified.

Recent field observations, laboratory and ab initio studies have prompted renewed efforts in understanding the DMS oxidation mechanism, with implications for constraining the uncertainty in the oxidation mechanism of DMS as incorporated in global chemistry-climate models. Here we build on recent evidence and develop a new DMS mechanism for inclusion in the UK Chemistry Aaerosol (UKCA) chemistry-climate model. We compare our new mechanism (CS2-HPMTF) to a number of existing mechanisms used in UKCA (including the highly simplified 3 reactions, 2 species, mechanism used in CMIP6 studies with the model) and to a range of recently developed mechanisms reported in the literature through a series of global and box model experiments. Global model runs with the new mechanism enable us to simulate the global distribution of hydroperoxyl methyl thioformate (HPMTF), which we calculate to have a burden of 2.6-26 Gg S (in good agreement with the literature range of 0.7-18 Gg S). We show that the sinks of HPMTF dominate uncertainty in the budget, not the rate of the isomerisation reaction forming it, and that based on the observed DMS/HPMTF ratio from the global surveys during the NAS Atmospheric Tomography mission (ATom), rapid cloud uptake of HPMTF worsens the model-observation comparison. Our box model experiments highlight that there is significant variance in simulated secondary oxidation products from DMS across mechanisms used in the literature, with significant divergence in the sensitivity of the rates of formation of these products to

34 temperature exhibited; especially for methane sulfonic acid (MSA). Our global model studies show that our updated DMS
35 scheme performs better than the current scheme used in UKCA when compared against a suite of surface and aircraft
36 observations. However, sensitivity studies underscore the need for further laboratory and observational constraints.

37 **1 Introduction**

38 It is estimated that 16-28 Tg S year^{-1} are emitted in the form of dimethyl sulfide (DMS, CH_3SCH_3) from the ocean, making
39 DMS the most abundant biological source of sulfur in the Earth system (Andreae, 1990, Tesdal et al., 2015, Bock et al., 2021).
40 Elucidating the atmospheric fate of DMS has been a long standing goal of the atmospheric chemistry research community
41 owing to a proposed biogeochemical feedback cycle (CLAW; Charlson et al. 1987), whereby DMS oxidation is key to a
42 homeostatic feedback loop. The initial steps in DMS oxidation are well understood (Barnes et al., 2006). Focusing on oxidation
43 via OH (NO_3), the most important oxidant during the daytime (nighttime), DMS is oxidised in the gas-phase through two main
44 pathways: the abstraction pathway forms the methylthiomethylperoxy radical (MTMP, CH_3SCH_2OO) in the first step, while
45 the addition pathway leads to dimethyl sulfoxide (DMSO, CH_3SOCH_3; and to a lesser extent $DMSO_2$) as an important
46 intermediate.
47 DMS + OH/$NO_3 \rightarrow$ MTMP + H_2O/HNO_3 (abstraction)
48 DMS + OH $\rightarrow$ DMSO + HO_2 (addition)
49 Ultimately, the oxidation of DMS leads to products such as H_2SO_4 and sulfate (SO_4^{2-}), as these represent the highest oxidation
50 states of sulfur (S(VI)). Along the way from DMS, a number of secondary oxidation products such as sulfur dioxide (SO_2),
51 methane sulfonic acid (MSA, CH_3SO_3H) and carbonyl sulfide (OCS) can be formed, however the yields of these species
52 depend on the mechanisms involved, which themselves are a function of the chemical (e.g., levels of oxidants) and
53 environmental conditions (e.g., temperature and humidity). The yields of these products are relatively uncertain, with estimates
54 of the DMS-to-SO_2 yield spanning 14-96 % (von Glasow and Crutzen, 2004). The oxidation products can participate in aerosol
55 growth and in new particle formation, affecting the number of cloud condensation nuclei (CCN). As such DMS oxidation can
56 impact cloud formation and lifetime and hence climate; although the absolute effect is still highly uncertain due to the
57 uncertainty in the kinetics and mechanisms of DMS oxidation. Indeed, natural aerosols such as DMS contribute to large
58 uncertainties in the radiative forcing of the pre-industrial atmosphere (Carslaw et al., 2013; Fung et al., 2022).
59
60 Substantial discrepancies between different DMS oxidation mechanisms under different conditions have been found (de Bryn
61 et al., 2002; von Glasow and Crutzen, 2004). The intercomparison study by Karl et al. (2007) looked at seven different
62 chemistry schemes in a box model (using the same inputs) and observed that SO_2 mixing ratios varied from 2 to 44 ppt.
63 Differences between models are even greater when looking at MSA yield (Karl et al., 2007, Hoffmann et al., 2021). The large
64 uncertainties of product ratios indicate the need for more observational constraints for DMS chemistry in models.

65   In the UK Chemistry and Aerosol model (UKCA) two different chemistry schemes are implemented: StratTrop (Archibald et

66   al., 2020), which is a simplified chemistry mechanism included in the UK Earth System Model (Sellar et al., 2019) and CRI-

67   Strat2 (Archer Nicholls et al., 2021; Weber et al., 2021). The DMS oxidation mechanism in StratTrop is, like those used in

68   many Earth System Models (ESMs), a very simple scheme (see S1.4.1 for more details). We believe modellers have opted to

69   keep the DMS chemistry incredibly simple for two main reasons 1) numerical efficiency 2) uncertainty in what to do owing

70   to lack of detailed DMS oxidation mechanisms that have been calibrated against laboratory data. The StratTrop DMS

71   mechanism only includes four reactions and no intermediates for the DMS oxidation scheme.

72   (R1) $DMS + OH \rightarrow SO_2 + MSA$

73   (R2) $DMS + OH \rightarrow SO_2$

74   (R3) $DMS + NO_3 \rightarrow SO_2$

75   (R4) $DMS + O(^3P) \rightarrow SO_2$
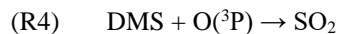
76   Omitting intermediates might lead to a misrepresentation of the spatial distribution of oxidation products and an overestimation

77   in their formation since the intermediates might be subject to wet and dry deposition or cloud uptake. Because a unity yield of

78   SO_2 is assumed, a change in the distribution of oxidation products due to a changing climate cannot be evaluated.

79

80   CRI-Strat2 (hereafter CS2) (Archer-Nicholls et al., 2021, Weber et al., 2021) is a mechanism that aims to be of intermediate

81   complexity. CS2 includes 19 reactions and 7 intermediates (DMSO, MSIA, MTMP, CH_3S, CH_3SO, CH_3SO_2, CH_3SO_3) as part

82   of its DMS scheme and is primarily based on the work of von Glasow and Crutzen (2004). Whilst the CS2 DMS mechanism

83   is much more complex than the StratTrop scheme, it represents an understanding of DMS chemistry that is far from up-to-

84   date.

85

86   In this work, the gas-phase DMS oxidation by OH and NO_3 in CS2 is updated according to the current scientific understanding.

87   The greatest update is the inclusion of the recently discovered intermediate hydroperoxymethyl thioformate (HPMTF,

88     $HOOCH_2SCHO$), which is formed through the autoxidation of the methylthiomethyl peroxy radical (MTMP, CH_3SCH_2OO)

89   in the abstraction pathway (Wu et al., 2015, Berndt et al., 2019, Veres et al. 2020). Currently, it is estimated that ~30-50% of

90   DMS yields HPMTF (Veres et al., 2020; Novak et al. (2021); Fung et al. (2022)). There are large uncertainties about the value

91   of $k_{isom,1}$, the rate constant of the first H-shift, which is the rate determining step for HPMTF formation (**Figure 1**). (Note, given

92   that he first isomerization step is rate limiting, the overall rate constant for isomerization is denoted k_{isom}). This determines if

93   autoxidation can compete with or surpass the bimolecular reactions of MTMP with HO_2 and NO. The chamber study by Ye et

94   al. (2021) estimates a probability distribution based on their measurements with one geometric standard deviation spanning an

95   order of magnitude. The isomerization rate constant is predicted using *ab initio* methods to be strongly temperature dependent,

96   indicating that this pathway could be more relevant under a warming climate (Wu et al., 2015; Veres et al., 2020). Following

97   the closure of the Discussion version of this manuscript the first temperature-dependent direct kinetic study of the isomerization

98   of rate constant for MTMP to HPMTF was published (Assaf et al., 2023). In that study the authors calculate the Arrhenius

99   temperature barrier as 7278 ± 99 K, confirming the high temperature dependence of the reaction experimentally.

100

101   As of now, the fate of HPMTF in the atmosphere is largely unknown. Wu et al. (2015) postulate further oxidation with OH,

102   ultimately yielding SO_2 as the dominant product and OCS as a side product. Veres et al. (2020) observe an abrupt decrease of

103   HPMTF mixing ratio in clouds and therefore suggest that heterogeneous loss to aerosol and cloud uptake plays a big role.

104   Vermeuel et al. (2020) support this hypothesis: they find a diurnal profile of HPMTF in the vicinity of California's coast and

105   suggest this is due to the consistent diurnal profile of cloud present. This hypothesis is further supported by the study by Novak

106   et al. (2021), which looks at two case studies and concludes that cloud uptake determines the lifetime of HPMTF. Novak et

107   al. (2021) found that cloud-uptake of HPMTF reduces SO_2 production from DMS by over a third, while providing a more

108   direct pathway to sulfate formation. On the contrary, the chamber study and calculation of Henry's law constant by Wollesen

109   de Jonge et al. (2021) predict that HPMTF does not directly contribute to new particle formation or aerosol growth. Instead,

110   their study proposes aqueous oxidation by OH, ultimately still yielding gas-phase SO_2. Khan et al. (2021) stress the importance

111   of photolysis as a potential loss pathway, which might explain the observed diurnal concentrations throughout the day. Overall,

112   loss processes of HPMTF are poorly understood.

113

114   In this work, we perform a series of updates to the CS2 DMS oxidation scheme which are evaluated against the current CS2

115   and the very simplified DMS chemistry in StratTrop. The aim of this work is to improve the representation of DMS chemistry

116   in UKCA and determine the influence of some of the major mechanistic uncertainties on model simulated SO_2 levels compared

117   against ATom observations (Wofsy et al., 2018; Veres et al., 2020). Our study includes a comprehensive set of box model

118   studies, including an intercomparison of our new DMS scheme against other recently reported schemes in the literature, and

119   global 3D simulations with the UKCA model. To complement the work of Fung et al. (2022), sensitivity studies with variable

120   rates of production, and cloud and aerosol uptake of HPMTF are performed to investigate the effects of the uncertainty in

121   HPMTF formation and depletion on the distribution and burden of SO_2 and sulfate (given their importance in climate) using

122   a structurally different model to that they used.

123

124 **2 Methods**

125 **2.1 Model description**

126 **2.1.1 Set up**

127 **Box model**

128 For the box model experiments, BOXMOX (Knote et al., 2015), the box modelling extension to the Kinetic PreProcessor

129 (KPP) (Sandu and Sander, 2006) was used. The initial and background concentrations of the species were set to be

130 representative of the remote marine boundary layer (MBL) (and are detailed in **Table S1**). NO_x concentration was kept at

131 approximately 10 ppt, unless otherwise specified.

132 The box model set up simulates an MBL air parcel exchanging with the free troposphere. The diurnal profile of the planetary

133 boundary layer height was modelled after the diurnal profile of the MBL in Ho et al. (2015) (**Table S2**). Mixing of the air

134 within the box with the free troposphere is described by the increases of box height: it is assumed that changes in the box

135 volume are due to the influx of background air. Emissions of DMS are added at 3.48×10^9 molec. cm^{-2} s^{-1} (consistent with

136 von Glasow and Crutzen, 2004). Emissions mix instantaneously within the box. Temperature varies throughout a 24-hour

137 period between 289-297 K, with a mean of 293 K (**Table S2**). Photolysis reactions are scaled depending on the time of day,

138 and make use of the pre-calculated "J" rates obtained from the MCMv3.3.1. The simulations were run for 192 hours (8 days)

139 with 10-minute time steps. CRI v2.2 R5 (CS2) (Jenkin et al., 2019; Weber et al., 2021) was employed as the base chemical

140 mechanism. Unless otherwise specified, only reactions of the DMS scheme were changed. Neither dry nor wet deposition was

141 included in the box model experiments. The analysis of the BOXMOX simulations discussed in Section 3.1.1 and 3.2.1 focuses

142 on the continuous (hourly) output. In Section 3.1.2 and 3.2.2, simulations with a prescribed temperature (260 - 310 K, step

143 size: 5 K) were conducted. The data from day 7 and 8 of the runs was averaged to enable the effects of changes in the

144 temperature on species concentration simulated in the box model to be calculated (following Archibald et al., 2010)

145

146 **3D simulations**

147 For the 3D simulations we use UKCA, the chemistry and aerosol component of UKESM1, with a horizontal resolution of

148 1.25°×1.875° with 85 vertical levels up to 85 km (Walters et al., 2019). UKCA uses the GLOMAP-mode aerosol scheme,

149 which simulates sulfate, sea salt, black carbon (BC), organic matter, and dust but does not currently simulate nitrate aerosol

150 (Mulcahy et al., 2020). Simulations were run for 18 months, using the first 6 months as spin up. In order to look at high time

151 resolution output simulations were re-run for limited time periods using the re-start files of the longer runs but outputting data

152 at hourly frequency.

153

154 Temperature and horizontal wind fields were nudged (Telford et al., 2013) in all model runs to the Era-Interim atmospheric

155 reanalysis from ECMWF (Dee et al., 2011). See the SI for further details.

156

157   The emissions used in this study for UKCA are the same as those from Archer-Nicholls et al (2021) and are those developed
158   for the Coupled-Model Intercomparison Project 6 (CMIP6) (Collins et al., 2017). See the SI for further details. Oceanic
159   emissions of DMS are calculated from seawater DMS concentrations (Sellar et al., 2019). In the atmosphere-only setup
160   employed here seawater DMS concentrations for 2014 from a UKESM1 fully-coupled SSP3-70 ensemble member were
161   prescribed. The DMS emission flux from the ocean used in the model was 16 Tg S yr^{-1} and therefore on the low end of estimates
162   of oceanic DMS emissions (e.g., Lana et al., 2011; Bock et al., 2021).

163

164

165   **2.1.2 Model runs**

166

167   **Table 1:** Configuration of model runs in this study. The last two columns indicate whether this scheme was used for the
168   BOXMOX experiments or the UKCA runs or both. Additional BOXMOX simulations were performed and the results of which
169   are included in the Supplementary Information (SI) for completeness.

Alias	Description	Used for: BOXMOX	UKCA
CS2	Base simulation, standard CRIStrat2 (or CRIv2.2R5) scheme	✓	✓
ST	StratTrop chemistry scheme *(ST - CS2 = ΔST; change between ST and CS2)*	✓	✓
ST~CS2	StratTrop DMS scheme but CS2 oxidants *(ST~CS2 - CS2 = ΔCC; change between CS2 and the ST DMS scheme only)*	✓	-
CS2-HPMTF	CS2 + updates in **Table 2** and **Table 3** *(CS2-HPMTF - CS2 = ΔUPD; effects of all updates made to the scheme)*	✓	✓
CS2-UPD-DMS	CS2 + updates in **Table 2** = CS2-HPMTF - updates in **Table 3** *(CS2-HPMTF - CS2-UPD-DMS = ΔHPMTF; effects of the isom. pathway only)*	✓	-
CS2-HPMTF-CLD	CS2-HPMTF + cloud and aerosol uptake (γ = 0.01) *(CS2-HPMTF-CLD - CS2-HPMTF = ΔCLD; gives the effects of cloud and aerosol uptake of HPMTF)*	-	✓
CS2-HPMTF-FL	CS2-HPMTF + faster total loss of HPMTF to OH (5.5×10^{-11} s^{-1}) *(CS2-HPMTF-FL - CS2-HPMTF = ΔFL; gives the effects of faster gas phase loss of HPMTF)*	SI	✓
CS2-HPMTF-FP	CS2-HPMTF + isomerisation *A*-factor scaled by a factor of 5, see Wollesen de Jonge et al. (2021)) *(CS2-HPMTF-FP - CS2-HPMTF = ΔFP; gives the effects of faster HPMTF production)*	SI	✓

170

171   Simulations are performed with the standard or updated DMS scheme to quantify the impacts of the mechanistic changes.

172   Details are given in **Table 1**. We chose as our base run a simulation with the CRIStrat2 chemistry scheme hereafter referred

173   to as CS2 (Weber et al., 2021). We perform two simulations with StratTrop (hereafter ST): ST is the default mechanism as

174   used in UKESM1, while ST~CS2 uses the ST DMS chemistry (R1-R4) but all other reactions (HO_x, NO_x, VOC etc) are

175   identical to CS2. This allows us to attribute the changes arising solely to differences in the oxidising capacity/environment

176   (driven by the chemistry not strongly coupled to DMS) and isolate the role due to differences in the DMS reactions themselves.

177

178   In updating the representation of DMS chemistry for UKCA a number of changes were considered. Broadly these fall into two

179   categories: 1) Incorporation of the chemistry of HPMTF (shown in red in **Figure 1**) 2) updates to other aspects of DMS

180   oxidation chemistry (shown in blue in **Figure 1**). CS2-HPMTF is used to identify the fully updated DMS mechanism (**Table**

181   **2**, **Table 3**). All other runs act as sensitivity runs. CS2-UPD-DMS allows the evaluation of only updating the standard DMS

182   chemistry (**Table 2**), without the addition of the isomerization branch and HPMTF formation (**Table 3**). CS2-HPMTF-CLD

183   adds cloud and aerosol uptake of HPMTF with subsequent sulfate formation, similar to Novak et al. (2021). With CS2-

184   HPMTF-FP and CS2-HPMTF-FL the effects of faster production and faster loss of HPMTF can be assessed.

185

186
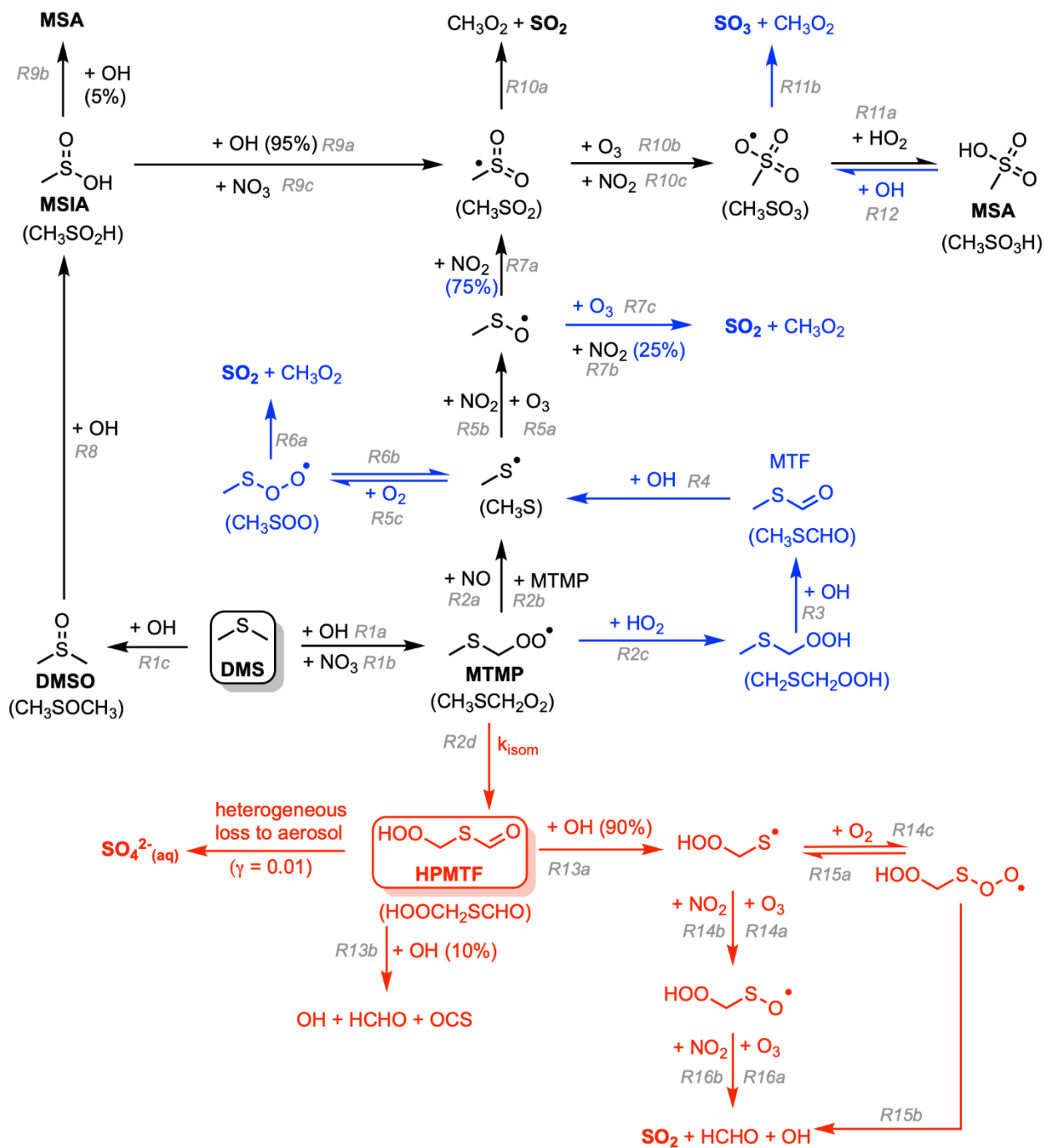
Figure 1. Schematic summary of the changes and additions to the gas-phase DMS oxidation mechanism in CS2. The current chemistry in CS2 (Weber et al., 2021) is in black, changes associated with CS2-UPD-DMS are shown in blue and changes associated with the addition of the isomerization pathway for CS2-HPMTF in red.

2.2 New mechanism development

192

193 The current CS2 DMS oxidation mechanism is based on von Glasow and Crutzen (2004). This mechanism is based on an
194 outdated understanding of DMS oxidation, which excludes key pathways and intermediates that are now known to be well
195 established (Barnes et al., 2006) as well as more recent pathways and products that have been shown to be important (Veres
196 et al., 2020). Our aim with the development of the new mechanism is to build upon the existing mechanism in CS2 and to
197 update and extend it. To this end we performed a literature review and constructed a number of mechanistic variants that were
198 examined in a series of box model experiments. As with all mechanism development exercises a series of target compounds
199 were chosen to reduce the mechanism to achieve a scheme that is parsimonious; for use in a 3D chemistry-climate model. In
200 our study we chose DMS, SO_2, sulfate and HPMTF as the key target molecules for mechanism optimization. **Figure 1** shows
201 the two-step improvement of this mechanism. First, the improvement of the standard chemistry by updating rate constants for
202 existing reactions in the scheme or the addition of reactions that were missing (denoted with blue colouring in **Figure 1**), and
203 second, the addition of the HPMTF pathway (in red in **Figure 1**). The focus in this study is on gas-phase DMS oxidation by
204 OH and NO_3. Our prime focus is on the primary oxidation products (DMSO and MTMP) and their subsequent chemistry.
205 While other studies include DMS oxidation by BrO and Cl, the contribution is either negligible or there is a large uncertainty
206 attached due to substantial discrepancies between/within models and measurements of halogens and halogen oxides (Wang et
207 al., 2021; Fung et al., 2022). Moreover, UKCA doesn't currently have a comprehensive tropospheric halogen mechanism and
208 levels of BrO and Cl simulated are much lower than observations suggest.

209

2.2.1 Updating the standard DMS chemistry in CRIStrat 2

210

211 The H-abstraction pathway (reaction 1a,b) generates MTMP which is then further oxidised to SO_2 or CH_3SO_2 (reactions 2-7).
212 The OH-addition pathway (reaction 1c) leads to dimethyl sulfoxide (DMSO, $(CH_3)_2SO$) and methanesulfinic acid (MSIA,
213 $CH_3S(O)OH$) (reactions 8,9) and further oxidation through to CH_3SO_2 (reactions 10-12). Both pathways and the changes made
214 are summarised in **Table 2**. The newly added reactions and their respective rate constants are largely based on Atkinson et al.
215 (2004), the MCMv3.3.1 (Jenkin et al. 2015), and the primary literature therein.

216

217 The oxidation of MTMP by HO_2 (reaction 2c) was not previously included in the CS2 mechanism, but is expected to play a
218 significant role at the low NO_x conditions over the remote ocean. Based on other $RO_2 + HO_2$ reactions, CH_3SCH_2OOH is the
219 expected product, which has been detected through mass spectroscopy (Butkovskaya and LeBras, 1994). Since no experimental
220 measurements exist for the kinetics of this reaction, the rate constant provided in the MCM was used. It is based on a generic
221 expression, defined on the basis of available room temperature and temperature dependent data for alkyl and β-hydroxy RO_2
222 and it is dependent on the number of carbon atoms. Further oxidation of CH_3SCH_2OOH leads to the formation of
223 methylthiolformate (MTF, CH_3SCHO) (reaction 3), a species that has been detected in chamber studies before under low NO_x

224   conditions (Arsene et al., 1999, Urbanski et al., 1998). MTF decomposes to CH_3S (reaction 4), an intermediate that is already
225   part of the CS2 DMS scheme as a reaction product of MTMP (reaction 2a,b).

226

227   CH_3S can add an O_2 to form a weakly bound adduct, CH_3SOO (reaction 5c). At 298 K at sea level, approximately one-
228   third of CH_3S is present as the CH_3SOO adduct and at colder temperatures this ratio is even greater (75% at 273 K)
229   (Turnipseed et al., 1992). CH_3SOO can decompose to CH_3 and SO_2 (reaction 6a), which proceeds through isomerization
230   to CH_3SO_2, followed by rapid thermal decomposition (McKee, 1993, Butkovskaya and Barnes, 2002, Chen et al. 2021).
231   Previous modelling studies, such as Hoffmann et al. (2016), include the isomerization step forming CH_3SO_2 but omit the
232   decomposition. This could lead to a higher yield of MSA in those studies.

233

234   CH_3S can also be oxidised by O_3 and NO_2 to CH_3SO (reaction 5a,b). Measurements by Borissenko et al. (2003) show that
235   O_3 oxidation of CH_3SO results in a 100% yield of SO_2 at pressures over 500 Torr (0.6 bar). Since the pressure in the marine
236   boundary layer where most of DMS oxidation takes place is above this threshold, the products of reaction 7c_old were
237   updated accordingly (reaction 7c). Additionally, the branching ratios of CH_3SO oxidation by NO_2 to CH_3SO_2 and SO_2
238   were revised to also match the findings by Borissenko et al. (2003).

239

240   While some CH_3SO_2 stems from the NO_3 oxidation of CH_3SO, it is mainly formed through oxidation of MSIA (reaction
241   9a,c), especially under low NO_x conditions. CH_3SO_2 can decompose to SO_2 (reaction 10a) or be oxidised further by O_3 or
242   NO_3 to CH_3SO_3 (reaction 10b,c). CH_3SO_3 itself can react to form MSA (reaction 11a). CH_3SO_3 can also decompose to
243   SO_3, similar to the decomposition reaction of CH_3SO_2, although it is assumed that this reaction is more endothermic
244   (Barone et al., 1995). The rate constant cited by von Glasow and Crutzen (2004) that was previously implemented in CS2,
245   could not be found in the cited primary literature (reaction 11b_old). Here, the rate constant of the decomposition reaction
246   was updated to the rate constant used in the MCMv3.3.1, which is — as for the decomposition of CH_3SO_2 — based on
247   Barone et al. (1995). We note that a more recent study, by Cao et al. (2013), calculates the rate constant for the thermal
248   decomposition of CH_3SO_3 to be 12 s^{-1}; a factor of 80 larger than the value adopted here based on the MCMv3.3.1.

249

250   MSA is formed either through oxidation of MSIA (reaction 9b) or through the reaction of HO_2 with CH_3SO_3 (reaction
251   11a). The default configuration of UKCA (for example as run in UKESM1) does not include any sinks for MSA and it is
252   not treated as a species, which prevents the comparison of MSA concentrations with observational results. Here, wet
253   deposition of MSA is added with a Henry's law coefficient of 1×10^9 M atm^{-1} (Campolongo et al., 1999; Sander 2021).
254   We note that Wollesen de Jonge et al. (2021) calculated the Henry's law coefficient to be approximately an order of
255   magnitude lower and so this might be an overestimate. Dry deposition for MSA is added based on the implemented values
256   for HCOOH in CRI. Additionally, the gas-phase oxidation of MSA by OH is added. Barnes et al. (2006) suggest this
257   pathway is expected to play a minor role.

258

259   Wet deposition was added for MSIA with Henry's law constant of 1×10^8 M atm^{-1} (Barnes et al., 2006). Dry deposition is

260   omitted for DMSO and MSIA since they are expected to be relatively short-lived.

261

262

263   **Table 2:** Summary of the H-abstraction and OH-addition branches in the DMS oxidation pathway. Reactions in **bold** are

264   newly added in this work.

No.	Reactions	Rate (cm^3 molecule^{-1} s^{-1})	Reference
1a	DMS + OH → MTMP + H$_2$O	1.12×10^{-11} exp$^{(-250/T)}$	IUPAC SOx22 (upd. 2006)
1b	DMS + NO$_3$ → MTMP + HNO$_3$	1.90×10^{-13} exp$^{(520/T)}$	Atkinson et al. (2004)
1c	DMS + OH → DMSO + HO$_2$	see note[a]	IUPAC SOx22 (upd. 2006)
2a	MTMP + NO → HCHO + CH3S + NO2	4.90×10^{-12} exp$^{(263/T)}$	von Glasow and Crutzen (2004)
2b	MTMP + MTMP → 2 HCHO + 2 CH$_3$S	1.0×10^{-11}	von Glasow and Crutzen (2004)
2c	**MTMP + HO$_2$ → CH$_2$SCH$_2$OOH**	$\mathbf{2.91\times10^{-13}}$ **exp**$^{\mathbf{(1300/T)}}$ **× 0.387**	MCMv3.3.1
3	**CH$_2$SCH$_2$OOH + OH → CH$_3$SCHO**	$\mathbf{7.03\times10^{-11}}$	MCMv3.3.1
4	**CH$_3$SCHO + OH → CH$_3$S + CO**	$\mathbf{1.11\times10^{-11}}$	MCMv3.3.1
5a	CH$_3$S + O$_3$ → CH$_3$SO	1.15×10^{-12} exp$^{(432/T)}$	Atkinson et al. (2004)
5b	CH$_3$S + NO$_2$ → CH$_3$SO + NO	3.00×10^{-12} exp$^{(210/T)}$	Atkinson et al. (2004)
5c	**CH$_3$S + O$_2$ → CH$_3$SOO**	$\mathbf{1.20\times10^{-16}}$ **exp**$^{\mathbf{(1580/T)}}$ **× [O$_2$]**	Atkinson et al. (2004)
6a	**CH$_3$SOO → CH$_3$O$_2$ + SO$_2$**	$\mathbf{5.60\times10^{+16}}$ **exp**$^{\mathbf{(-10870/T)}}$	Atkinson et al. (2004)
6b	**CH$_3$SOO → CH$_3$S + O$_2$**	$\mathbf{3.50\times10^{+10}}$ **exp**$^{\mathbf{(-3560/T)}}$	MCMv3.3.1 (based on: McKee (1993), and Butkovskaya and Barnes (2002))
7a	CH$_3$SO + NO$_2$ → CH$_3$SO$_2$ + NO	1.2×10^{-11} × **0.75**	Borrisenko et al. (2003), Atkinson et al. (2004)
7b	CH$_3$SO + NO$_2$ → SO$_2$ + CH$_3$O$_2$ + NO	1.2×10^{-11} × **0.25**	Borrisenko et al. (2003), Atkinson et al. (2004)
7c_old	CH$_3$SO + O$_3$ → CH$_3$SO$_2$	6.0×10^{-13}	Von Glasow and Crutzen (2004)
7c	**CH$_3$SO + O$_3$ → CH$_3$O$_2$ + SO$_2$**	$\mathbf{4\times10^{-13}}$	Borrisenko et al. (2003), IUPAC SOx61 (upd. 2006)
8	DMSO + OH → MSIA + CH$_3$O$_2$	8.7×10^{-11} × 0.95	von Glasow and Crutzen (2004)
9a	MSIA + OH → CH$_3$SO$_2$ + H$_2$O	9.0×10^{-11} × 0.95	von Glasow and Crutzen (2004)
9b	MSIA + OH → MSA + HO$_2$ + H$_2$O	9.0×10^{-11} × 0.05	von Glasow and Crutzen (2004)
9c	MSIA + NO$_3$ → CH$_3$SO$_2$ + HNO$_3$	1.0×10^{-13}	von Glasow and Crutzen (2004)
10a	CH$_3$SO$_2$ → CH$_3$O$_2$ + SO$_2$	5.0×10^{-13} exp$^{(-9673/T)}$	MCMv3.3.1 (based on: Barone et al. (1995))
10b	CH$_3$SO$_2$ + O$_3$ → CH$_3$SO$_3$	3.0×10^{-13}	von Glasow and Crutzen (2004)
10c	CH$_3$SO$_2$ + NO$_2$ → CH$_3$SO$_3$ + NO	2.2×10^{-12}	Atkinson et al. (2004)
11a	CH$_3$SO$_3$ + HO$_2$ → MSA	5.0×10^{-11}	von Glasow and Crutzen (2004)
11b_old	CH$_3$SO$_3$ → CH$_3$O$_2$ + H$_2$SO$_4$	1.36×10^{14} exp$^{(-11071/T)}$	von Glasow and Crutzen (2004)
11b	**CH$_3$SO$_3$ → CH$_3$O$_2$ + SO$_3$**	$\mathbf{5.0\times10^{13}}$ **exp**$^{\mathbf{(-9946/T)}}$	MCMv3.3.1 (based on: Barone et al. (1995))

12	**MSA + OH → CH$_3$SO$_3$**	2.24×10^{-14}	MCMv3.3.1

265 [a] $9.5\times10^{-39}\exp^{(5270/T)}\times[O_2]$ / $(1+7.5\times10^{-29}\exp^{(5610/T)}\times[O_2])$

266

267 **2.2.2 The addition of the isomerization branch**

268 Following the discovery of HPMTF (Veres et al., 2020) the pathway forming this molecule has now been well established
269 (Wu et al., 2015; Veres et al., 2020; Berndt et al., 2019; Ye et al., 2021). The reactions of the isomerization branch that were
270 added to CS2 (summarised in **Figure 1** and **Table 3**) were identified as those most important in determining SO$_2$ and HPMTF
271 concentrations through sensitivity studies conducted using our box model setup. Details of these box model sensitivity studies
272 (and the discarded reaction pathways that were found to not be significant) are included in the supplement. In this sense,
273 species like HOOCH$_2$SCH$_2$OOH, included in the studies by Khan et al. (2021) were neglected from our mechanism as this
274 was found to have minor impact on the SO$_2$ and HPMTF simulated in the box model experiments. The reactions that were
275 added include the autoxidation of MTMP to HPMTF in one step (reaction 2d) and the oxidation of HPMTF by OH, forming
276 OCS (reaction 13b) and HOOCH$_2$S (reaction 13a) with further oxidation to SO$_2$ (reactions 14-16). The equilibrium with the
277 O$_2$-adduct, HOOCH$_2$SOO, and its subsequent decomposition (reaction 14c, 15a,b) was included with kinetics equivalent to
278 CH$_3$SOO (reaction 5c, 6a,b). Photolysis was found to be a minor pathway of HPMTF loss in our marine boundary layer box
279 model setup ($< 10\%$) and was omitted from the final mechanism used here; contrary to the importance of photolysis of HPMTF
280 found by Khan et al. (2021).

281

282 Dry deposition of HPMTF is set using the same parameters in UKCA as other soluble gas-phase compounds, such as CH$_3$OOH
283 and H$_2$O$_2$, which yield an average deposition velocity similar to the observations of Vermeuel et al. (2020) of 0.75 cms^{-1}. For
284 wet deposition of HPMTF, the Henry's law coefficient calculated by Wollesen de Jonge et al. (2021) was used.

285

286 For the sensitivity runs described in **Table 1**, some changes are made to the values in **Table 3**. In DMS-HPMTF-FP, the rate
287 constant of reaction 2d is scaled by a factor of 5.0: Berndt et al. (2019) experimentally determined the rate constant at 295 K
288 as 0.23 s^{-1}. Here the A-factor is scaled to match this value, while keeping the temperature dependence calculated by Veres et
289 al. (2020) (following Wollesen de Jonge et al. (2021)). DMS-HPMTF-FL uses a rate constant 5.5 times faster for the total loss
290 of HPMTF to OH (reaction 13a,b), which was recommended as an upper bound by Vermeuel et al. (2020) and following Khan
291 et al. (2021). This range, between the base rate constant and the faster loss, puts us in the middle of the value experimentally
292 determined by Ye et al. (2022). In the remaining sensitivity run CS2-HPMTF-CLD, heterogeneous uptake to both clouds and
293 aerosols was added with reactive uptake coefficient (γ) of 0.01 (following Novak et al., 2021).

294

295 **Table 3:** Summary of the isomerization branch of the H-abstraction pathway. Rate constants referenced to this work are
296 described in Section 2.2

No.	Reaction	Rate (cm^3 molecule^{-1} s^{-1})	Reference
2d	MTMP $\rightarrow$ HPMTF + OH	see note[a]	Veres et al. (2020)
13a	HPMTF + OH $\rightarrow$ HOOCH$_2$S + H$_2$O + CO	$1.0\times10^{-11} \times 0.9$	this work
13b	HPMTF + OH $\rightarrow$ OCS + OH + HCHO + H$_2$O	$1.0\times10^{-11} \times 0.1$	this work
14a	HOOCH$_2$S + O$_3$ $\rightarrow$ HOOCH$_2$SO	$1.15\times10^{-12} \exp^{(430/T)}$	Wu et al. (2015)
14b	HOOCH$_2$S + NO$_2$ $\rightarrow$ HOOCH$_2$SO + NO	$6.00\times10^{-11} \exp^{(240/T)}$	Wu et al. (2015)
14c	HOOCH$_2$S + O$_2$ $\rightarrow$ HOOCH$_2$SOO	$1.20\times10^{-16} \exp^{(1580/T)} \times$ [O$_2$]	this work
15a	HOOCH$_2$SOO $\rightarrow$ HOOCH$_2$S + O$_2$	$3.50\times10^{+10} \exp^{(-3560/T)}$	this work
15b	HOOCH$_2$SOO $\rightarrow$ HCHO + OH + SO$_2$	$5.60\times10^{-16} \exp^{(-10870/T)}$	this work
16a	HOOCH$_2$SO + O$_3$ $\rightarrow$ HCHO + OH + SO$_2$	4×10^{-13}	Wu et al. (2015)
16b	HOOCH$_2$SO + NO$_2$ $\rightarrow$ HCHO + OH + NO + SO$_2$	1.2×10^{-11}	Wu et al. (2015)

297   [a] $2.24\times10^{+11} \exp^{(-9800/T)} \exp^{(1.03e8/(T\times T\times T))}$

298

299 **2.3 Description of observational data**

300 **2.3.1 The NASA Atmospheric Tomography (ATom) mission**

301 An observational dataset used to compare with the model simulations stems from the fourth flight campaign of the NASA

302 Atmospheric Tomography mission (ATom-4). ATom-4 took place during April and May 2018, and completed a global circuit

303 around the Americas: from the Arctic to the Antarctic over the remote Pacific and Atlantic Ocean at varying altitudes up to 12

304 km. A vast number of atmospheric species were measured, including DMS, HPMTF, and SO$_2$ (Wofsy et al., 2018).

305

306 In order to compare the 3D model outputs with the data from the ATom-4 campaign, the hourly outputs from the respective

307 model runs were interpolated in regards to time and space to generate the data along the flight path. Only model data at times

308 where valid atmospheric measurements were available are taken into account, resulting in 313 data points for DMS (Whole

309 Air Sampling) and 36,652 for SO$_2$ (Laser Induced Fluorescence).

310

311 **2.3.2 Surface observations**

312 Other observational measurements are monthly averages (mean) from the years 1990 to 1999 for DMS measurements made

313 on Amsterdam Island (37°S, 77°E) in the southern Indian Ocean (Sciare et al., 2000) and the monthly means from 1991 to

314 1995 for sulfate at the Dumont d'Urville station (66°S, 140°E) at the coast of Antarctica (Minikin et al., 1998). The diel profile

315 of HPMTF as measured at Scripps Pier in July 2018 was taken from Vermeuel et al. (2020). See the SI for the analysis of the

316 modelled and observed DMS mixing ratios.

3 Comparison of DMS oxidation pathways (BOXMOX)

Here we present the results of a series of box model simulations using the BOXMOX model (Weber et al., 2020). With BOXMOX we look at the diversity in results from simulations using a range of mechanisms, including our newly developed mechanism. These simulations are not constrained to observations or simulation chamber data. The set-up of the BOXMOX simulations is described in Section 2.1.1. We focus the analysis here on DMS and its major oxidation products and the effects of temperature and [NO_x] on these. Section 3.1 compares DMS mechanisms based around the CS2 and ST schemes used in UKCA (**Table 1**). In Section 3.2 our newly developed mechanism is compared to other DMS mechanisms from recent literature that also include HPMTF formation.

3.1 Comparison of DMS mechanisms used for UKCA

3.1.1 Time series analysis

The BOXMOX set up allows a quasi steady-state to be achieved for a number of key sulfur species with the main exception being H_2SO_4, which builds up over time in the model as the model is run without aerosol formation and aerosol microphysics included (**Figure 2**). The DMS concentration simulated with different DMS mechanisms used in UKCA is simulated to be very similar throughout all model runs; the small variations stem from different oxidant concentrations or small differences in the rate constants used for the initiation reaction in the different mechanisms (**Figure 2a**). For instance, the ST run has higher DMS concentration because the NO_x concentration is lower (as is OH) and less DMS is oxidised.

The SO_2 concentration is increased and MSA is significantly decreased in the updated CS2 runs (CS2-HPMTF and CS2-UPD-DMS) compared to CS2 (**Figure 2b,c**). Comparing CS2-HPMTF and CS2-UPD-DMS, we can see that this pattern (increased SO_2 and decreased MSA) is due to reaction 7c, which directly forms SO_2 and suppresses CH_3SO_2, consequently lowering MSA formation. The SO_2 concentration is lower in CS2-HPMTF compared to CS2-UPD-DMS because the addition of HPMTF produces OCS which acts as a long-lived sulfur reservoir. While MSA concentration is very similar between CS2 and ST, SO_2 concentration is not. This is primarily explained through the difference in the treatment of MSA and SO_2 production in CS2 and ST. MSA is not treated as a reactive species in CS2 and ST (in so much as there are no further reactions of MSA after its production). In ST and ST~CS2, 100% of DMS yields SO_2, regardless of the amount of MSA production. However, as more MSA is produced in CS2 the SO_2 yield is lowered. In spite of higher SO_2 concentrations in the ST DMS schemes, this trend does not translate to H_2SO_4 concentration (**Figure 2d**). SO_2 is a relatively long-lived species (~2 days in our model but with a range from 0.5-2.5 days (Lee et al., (2011))) and can therefore be lost through the mixing processes with the background air in the BOXMOX setup. In CS2, CH_3SO_3 decomposition provides a direct pathway to H_2SO_4 production. In the updated CS2 schemes (CS2-UPD-DMS and CS2-HPMTF) SO_3 production with instantaneous transformation to H_2SO_4 is included. The slower rate constant in CS2 for the decomposition of CH_3SO_3 (11b_old) is compensated by a higher production of CH_3SO_3.

347
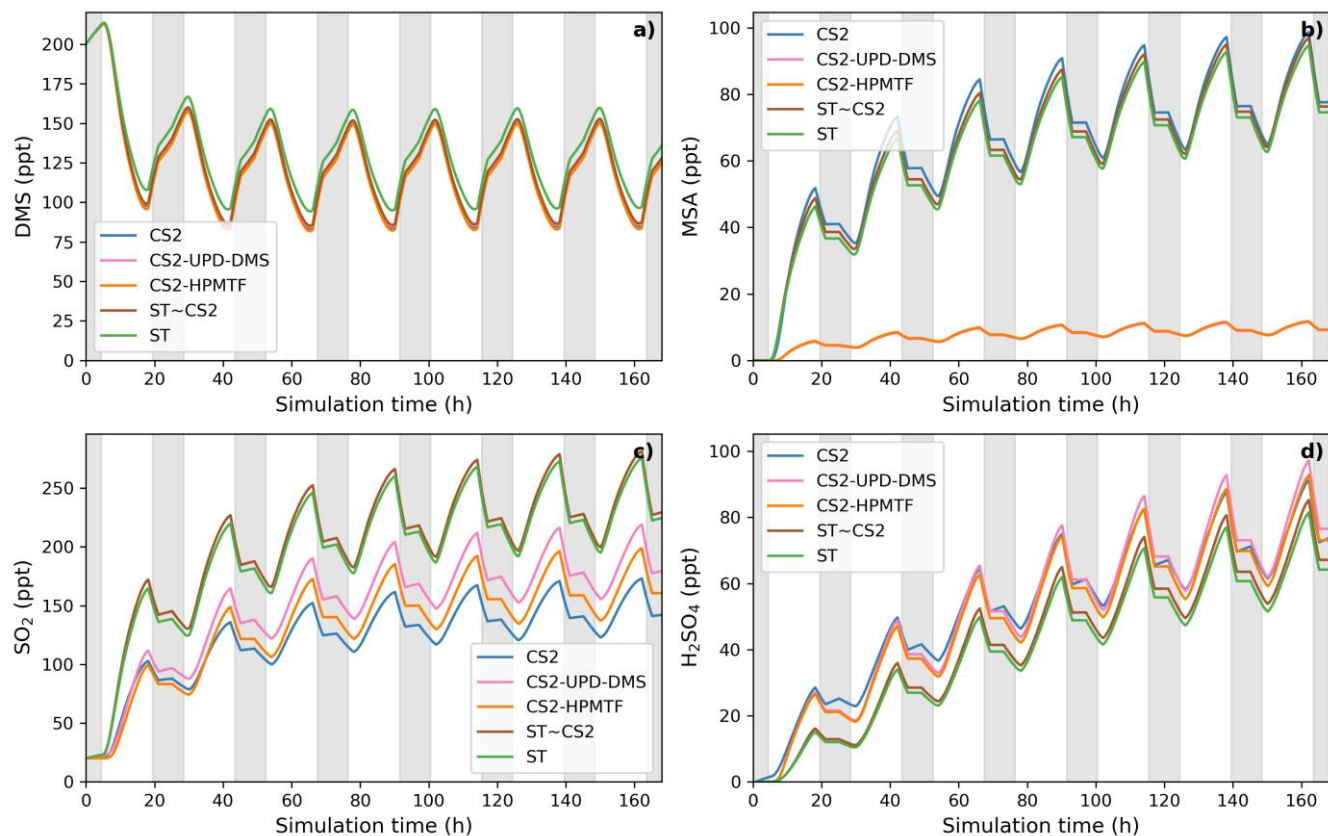
Figure 2: BOXMOX-simulated gas-phase concentrations as a function of time for a selection of species simulated with the different DMS gas-phase oxidation schemes used in UKCA configurations (oxidation by OH and NO$_3$). Grey areas denote nighttime, when no photolysis reactions are taking place. Average NO$_x$ concentration is approximately 10 ppt, with an average temperature of 293 K (range: 289 – 297 K).

352

3.1.2 Sensitivity of UKCA DMS schemes to temperature

As described in Section 2.1.1, a series of BOXMOX experiments were performed perturbing the temperature profile in the model (**Figure 3**).

356

As temperature increases in the box model, the steady-state DMS concentration increases in all simulations. This is mainly because the DMS oxidation by OH addition is negatively temperature dependent. For most models, DMS concentration increases by 85-93 ppt throughout the temperature range from 260 K to 310 K, except the ST run where at temperatures over 290 K, a stronger increase of DMS concentration is found, with a total increase of 106 ppt. This could be due to different

361 oxidant concentrations in the model runs using the ST mechanism and independent of the DMS scheme since this stronger

362 increase is not found with CS2-ST.

363 Although the kinetics, and therefore temperature dependence, of DMS loss is comparable across the different schemes, the

364 dependence of MSA and SO_2 on temperature differ significantly.

365

366 Most MSA is formed from the OH-addition channel, which is favoured at low temperatures (Barnes et al., 2006). Therefore,

367 the MSA concentration is higher at lower temperatures across all the UKCA DMS schemes considered (**Figure 3b**). In the ST

368 schemes (ST and ST~CS2), MSA decreases by around 88% (-189 ppt and -197 ppt) throughout the temperature range

369 considered, while in all the CS2 schemes MSA is shown to be much more sensitive to temperature, decreasing by >96% (CS2:

370 –300 ppt, CS2-UPD-DMS: -222 ppt, CS2-HPMTF: -222 ppt). In particular the CS2 family of mechanisms shows pronounced

371 temperature sensitivity between 270 to 290 K. We attribute this to differences in the rate constant of DMS oxidation through

372 the OH-addition channel (see **Table 2** and **S1.3.1**). The average MSA concentration for the UKCA schemes diverges most in

373 the temperature range between 270 - 300 K.

374

375 The difference in SO_2 concentrations between the CS2 schemes and ST schemes are greatest at lower temperature (**Figure

376 3c**), with the ST and CS2-ST schemes simulating ~ 5 times (+200 ppt) the SO_2 that is simulated in the other schemes based

377 around CS2. In the ST schemes SO_2 concentration either stays at a similar level across the whole temperature range (ST: +3%)

378 or slightly decreases (ST~CS2: -9%). Conversely, the CS2 family of schemes show a positive temperature dependence (i.e.,

379 $+\frac{d[X]}{dT}$), across the temperature range, especially in the range of relevant atmospheric temperatures from 270 to 290 K. SO_2

380 increases by 298% in CS2, 84% in CS2-UPD-DMS and 79% CS2-HPMTF. In the CS2 schemes, more DMS reacts through

381 the addition pathway which favours the production of MSA, instead of SO_2 therefore reducing the SO_2 concentration. In ST,

382 the addition pathway still leads to 100% SO_2 formation, making the average SO_2 concentration less dependent on temperature.

383 Experimental findings (Arsene et al., 1999) and field measurements (Sciare et al., 2001) both show a positive temperature

384 dependence of SO_2 concentration. This trend is only reproduced by the DMS schemes based on the CS2 mechanistic features

385 (i.e. not the very simple mechanism used in ST), indicating that the ST DMS chemistry is likely insufficient to explain

386 laboratory and field observations, particularly in cold environments and under climate change.

387

388 In these box model experiments only gas phase losses and mixing of species with background air are considered. Under the

389 conditions of our simulations, we find that the MTMP isomerization pathway mainly yields SO_2, as does the rest of the

390 abstraction pathway. Therefore, the addition of the isomerization branch does not have a significant impact on the temperature

391 dependence of SO_2 concentration (comparing CS2-UPD-DMS and CS2-HPMTF), even though the isomerization step itself is

392 greatly temperature dependent.
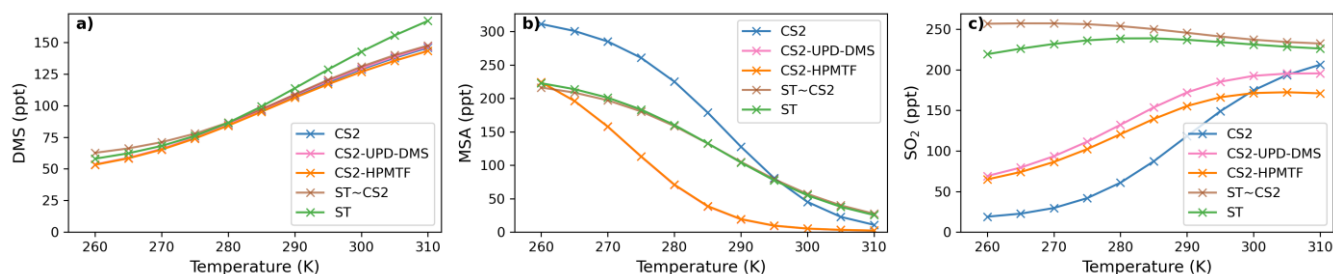
Figure 3: Temperature dependence of average a) DMS, b) MSA, and c) SO_2 concentration after a quasi steady-state is reached in the box model simulations using the DMS schemes for UKCA.

3.2 Comparison with DMS schemes that include HPMTF from the recent literature

Here, four recently published DMS schemes that also include the isomerization pathway and formation of HPMTF are compared with our new mechanism, CS2-HPMTF (*CS-H*, 36 reactions in DMS scheme), as follows. To make the studies comparable, only DMS oxidation by NO_3 and OH and gas-phase reactions are considered. The implementation of these chemical schemes in BOXMOX can be found in the *Supporting Information S1.3*.

- *Fung et al. (2022) (FG):* This scheme includes 32 reactions for the DMS oxidation chemistry. The H-abstraction pathway is based on the MCM, while the rate constants in the OH-addition pathway mostly stem from Burkholder et al. (2015) or a scaled up version of those. The rate constant of MTMP isomerization to HPMTF is based on Veres et al. (2020).
- *Wollesen de Jonge et al. (2021) (WJ):* This scheme is the most complex and consists of 98 reactions, including reactions from the MCM and from Hoffmann et al. (2016). The isomerization branch mostly uses the rate constants by Wu et al. (2015), except the first isomerization rate constant, which is a combination of Veres et al. (2020) and Berndt et al. (2019).
- *Khan et al. (2021) (KH):* This scheme is based on Khan et al. (2016), which is equivalent to the DMS chemistry in CS2 (CRI v2 R5). The mechanism was modified to include the isomerization pathway and photolysis loss and temperature dependent OH oxidation of HPMTF by the authors. In total, the DMS chemistry consists of 38 reactions, 5 of which are photolysis reactions.
- *Novak et al. (2021) (NV):* This is a simplified scheme that aims to only include the intermediates necessary for HPMTF formation and consists of only 10 reactions. DMS therefore either directly yields MSA (without DMSO formation) or first forms MTMP, which isomerizes to form HPMTF or is oxidised to SO_2.

418 Using this ensemble of gas-phase DMS oxidation schemes in BOXMOX simulations leads to significant differences in the

419 concentrations of important oxidation intermediates and products, even though DMS concentration is similar across all models

420 (**Figure 4**).

3.2.1 Time series analysis of different DMS-HPMTF schemes
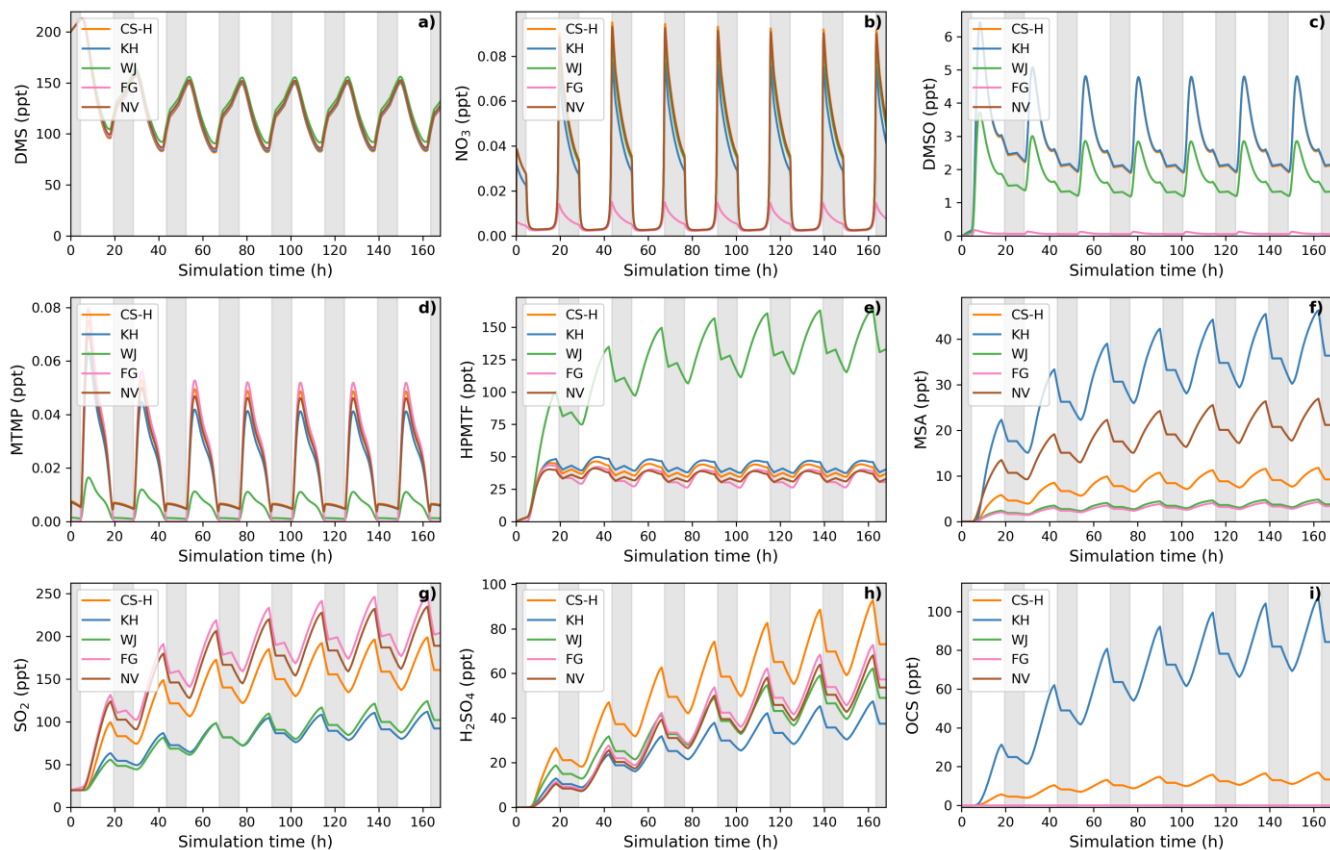
422
423 **Figure 4:** Gas-phase concentrations as a function of time for different DMS gas-phase oxidation schemes (oxidation by OH

424 and NO$_3$). Average NO$_x$ concentration is approximately 10 ppt, with an average temperature of 293 K (range: 289 – 297 K).

425 Grey areas denote nighttime when no photolysis reactions are taking place.

426

427

428 The depletion of DMS due to OH and NO$_3$ oxidation is similar across most models (**Figure 4a**) since the major oxidants are

429 relatively constrained by the box model experiment set up (see Section 2.1.1) and they mostly rely on IUPAC or JPL

430 recommended values (Atkinson et al., 2004; Burkholder et al., 2015). One exception is NO$_3$ oxidation in the FG scheme, which

431 uses a rate constant a factor of approximately 6 higher than the JPL recommendation. On the one hand, this does not affect

432 DMS concentration, since OH oxidation of DMS plays a greater role, on the other hand, the concentration of NO$_3$ in the FG

433 scheme's simulation run is controlled by the greater NO_3 oxidation rate (**Figure 4b**). WJ includes the intermediate

434 $CH_3S(OH)CH_3$ and its decomposition back to DMS (based on Hoffmann et al., (2016)), which in their experiments improved

435 the fit between their measured and modelled DMS concentration. Here, this does not have any significant impact on DMS

436 concentration, compared to all the other schemes.

437

438 Significant differences between the models can be found for the DMSO concentration (**Figure 4c**). KH and CS-H have the

439 highest DMSO concentration since all DMS that is oxidised through the OH-addition pathway yields DMSO. This is not the

440 case for WJ, where CH_3SOH and to a small part DMSO2 are also possible products. In the FG simulation, DMSO concentration

441 is close to zero, which is due to a much faster loss of DMSO; a rate constant a factor of 15 faster than experimental

442 measurements by Urbanski et al. (1998). NV does not include DMSO as an intermediate. Since the lifetime of DMSO was

443 found to be several hours (Urbanski et al., 1998; Ye et al. 2021), deposition of DMSO could act as a significant sink of

444 atmospheric sulfur (as found by Chen et al. (2018)). Fast oxidation of DMSO in FG, or omitting the species in NV, might

445 therefore lead to an over-estimation of other DMS oxidation products in those schemes.

446

447 Regarding the intermediate MTMP, WJ shows the greatest deviation from the ensemble (**Figure 4d**). The MTMP concentration

448 never exceeds 0.02 ppt in WJ, while the other mechanisms simulate concentrations over three times higher. WJ employs a

449 faster isomerization rate constant of MTMP to HPMTF. They scale the A-factor by 5 to get a rate constant that is a combination

450 of the theoretical calculations by Veres et al. (2020) and the experimental findings by Berndt et al. (2019). Additionally, they

451 include more oxidation reactions of MTMP (such as oxidation by NO_3) but since the isomerization to HPMTF already

452 outcompetes most oxidation reactions anyway (>97%), we found them to play a negligible role (<0.1%). In the FG scheme,

453 $DMS + NO_3$ leads to immediate SO_2 formation, without prior MTMP formation. Therefore, no MTMP is produced during the

454 nighttime, when NO_3 oxidation becomes relevant. Under conditions with low NO_x (around 10 ppt in this experiment) this does

455 not have significant impacts but at higher NO_x concentrations this leads to a major deviation from the other simulations (**Figure**

456 **5a**, 100 ppt NO_x). At night, CS-H, KH, and NV reach MTMP concentrations of 0.07 ppt, allowing nighttime HPMTF

457 formation, while FG stays zero.

458

459 All model simulations, except WJ, are very similar in HPMTF concentration (**Figure 4e**). The fast isomerization rate constant

460 in WJ is one of the reasons HPMTF concentration is on average more than 3 times higher than the other model simulations.

461 The other reason is a much slower oxidation of HPMTF by OH. While most models use a value of (or close to) 1.11×10^{-11}

462 cm^3 molecule^{-1} s^{-1}, recommended by Vermeuel et al. (2020), WJ use the much slower rate constant calculated by Wu et al.

463 (2015), 1.4×10^{-12} cm^3 molecule^{-1} s^{-1}. This rate constant is also used in the KH scheme but it additionally includes HPMTF

464 depletion by photolysis which ultimately leads to the similar HPMTF concentration as in CS-H, FG, and NV. The addition of

465 the photolysis reactions in KH does not affect the diel profile of HPMTF, even though those account for 81% of chemical loss

466 of HPMTF in their scheme. It is therefore unlikely that the observed diel profile of HPMTF by Vermeuel et al. (2020) and

467   Khan et al. (2021) can be explained solely by considering loss of HPMTF to aldehyde and hydroperoxide photolysis. Reducing

468   HPMTF formation to one isomerization reaction without any side reactions as is done in this work and NV, does also not affect

469   the diel profile of HPMTF significantly.

470   The effect of higher NO_x conditions on the diel profile of HPMTF varies significantly between the different schemes (10 ppt

471   NO_x in **Figure 4** vs. 100 ppt NO_x in **Figure 5**). Higher NO_x concentration leads to more DMS oxidation by NO_3 at night and

472   the subsequent increase in MTMP concentration and therefore HPMTF concentration during the night hours in the CS-H, WJ,

473   KH, and NV simulations. At low NO_x, HPMTF concentration stayed more or less stable throughout the nighttime and increased

474   in the morning, reaching a plateau in the afternoon, and dropping in the evening (**Figure 4e**). Under higher Nox conditions,

475   HPMTF increases in these mechanisms throughout the night and decreases throughout the day when it is oxidised by OH

476   (**Figure 5b**). In the WJ simulation, the diel profile has more plateaus and small deviances but the overall trend still fits the

477   described pattern. This is not true for FG, where DMS oxidation by NO_3 leads directly to SO_2 formation.

478
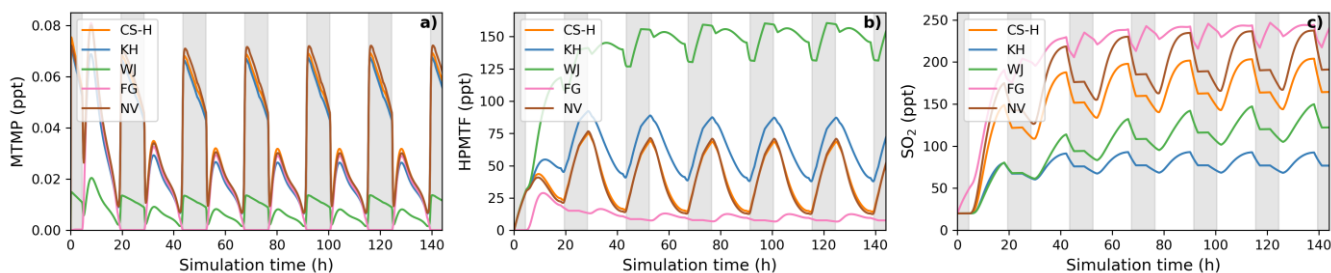
479

480   **Figure 5:** BOXMOX simulations where the average NO_x concentration is approximately 100 ppt (a factor 10 greater than for

481   the results presented in **Figure 4**). **(a)** MTMP, **(b)** HPMTF, and **(c)** SO_2 concentration as a function of time for different DMS

482   gas-phase oxidation schemes (oxidation by OH and NO_3). Average temperature of 293 K (range: 289 – 297 K). Grey areas

483   denote nighttime when no photolysis reactions are taking place.

484

485   While the diel profile of MSA looks similar for all simulations, the average concentrations do not (**Figure 4f**). The highest

486   average steady-state MSA concentration is reached in the KH simulation, which is a factor of 10 higher than the lowest average

487   concentration in the FG simulation. In our experimental setup, most of the simulations we performed with the different

488   mechanisms do not include any (significant) gas-phase chemical loss pathway for MSA; MSA is only lost through mixing and

489   transport out of the "box". Therefore, the concentration of MSA is a direct reflection of MSA production in the respective

490   simulations.

491

492   KH simulates the highest production of MSA (similar to CS2), where MSA is formed through the addition (MSIA + OH →

493   0.05 MSA + 0.95 CH_3SO_2, reaction 9b,c) and the abstraction channel ($CH_3SO + O_3$ → CH_3SO_2, reaction 7c_old) of DMS

494   oxidation, with CH_3SO_2 partly being oxidised to CH_3SO_3 and then to MSA (reactions 10b,c, 11a). The decomposition of

495 CH_3SO_3 to H_2SO_4 in KH is slower than in other mechanisms, increasing the branching ratio for MSA formation in their

496 mechanism. In NV, the simulation with the second highest average MSA concentration, the only source of MSA is the direct

497 production of MSA through OH oxidation through the addition channel, where 25% of DMS forms MSA. In both, CS-H and

498 WJ, the abstraction pathway mostly produces SO_2 and only contributes negligible amounts to CH_3SO_2 formation, hence MSA.

499 Similar to KH, the oxidation of DMS through the addition pathway in CS-H and WJ yields CH_3SO_2 of which a part forms

500 MSA. However, not all of the CH_3SO_2 results in MSA, some of it also decomposes to SO_2 or yields SO_3. This explains the

501 lower concentration of MSA in CS-H and WJ compared with NV. The reason why CS-H has a higher MSA concentration than

502 WJ is because of the inclusion of reaction 9b (**Table 2**), which yields MSA directly and is not part of the WJ scheme.

503 The lowest MSA concentration is found in FG and WJ, where 60% of the OH-addition pathway directly produces SO_2. Out of

504 the 40% of DMS that forms DMSO in this pathway, only a fraction yields MSA.

505

506 To harmonise the results and aid interpretability, the same rates (based on CS2) are used for the loss processes of SO_2 in all

507 the mechanisms considered here, therefore the concentration of SO_2 can be used as a proxy for SO_2 production, just as for

508 MSA. The highest SO_2 concentration can be seen in schemes that have the smallest number of intermediates or the most direct

509 pathways from DMS to SO_2, in NV and FG (**Figure 4g**). Fewer intermediates result in less opportunities for the formation of

510 side products or less long-lived species that can be lost through transport or deposition. For instance, in WJ HPMTF is lost

511 through mixing with the background before it can form SO_2. Likewise, KH has a higher ratio of MSA and OCS production,

512 which lowers the SO_2 yield. The diel profile of SO_2 concentration is in most simulations not affected by higher NO_x

513 concentrations, with the general trend being an increase of SO_2 concentration during the day and a decrease at night (**Figure**

514 **5c**). The only exception is the FG simulation, where we see a clear increase through part of the night, due to the reaction DMS

515 + $NO_3 \rightarrow SO_2$.

516

517 The H_2SO_4 concentration is influenced by SO_2 production and CH_3SO_3 production and the rate of decomposition of SO_3 to

518 H_2SO_4. CS-H has the highest average H_2SO_4 concentration and KH the lowest; all other models are very similar to each other

519 (**Figure 4h**). In general, higher SO_2 concentration leads to more H_2SO_4, since SO_2 is first oxidised to SO_3 and then to H_2SO_4

520 with the same rates across all schemes. However, all models except NV include an additional pathway of H_2SO_4 formation: in

521 KH and FG, H_2SO_4 is directly formed from CH_3SO_3, while in CS-H and WJ CH_3SO_3 decomposes to SO_3 first, which then

522 instantly reacts to H_2SO_4. In KH, the rate constant for the decomposition of CH_3SO_3 at 295 K is a factor of 15 slower than in

523 the other models. Since the SO_2 concentration is also relatively low, it explains why KH has the lowest H_2SO_4 concentration

524 of all schemes when reaching steady-state. CS-H results in a higher H_2SO_4 concentration than FG or NV even though those

525 models have a higher SO_2 concentration. The reason is a higher production of CH_3SO_3 that is then decomposed to SO_3 and

526 H_2SO_4.

527

528   Similar to the other products of the DMS scheme, the concentration of OCS is a reflection of its production. OCS is only

529   produced from oxidation of HPMTF by OH and, in the KH scheme, through photolysis of HPMTF. In KH, 60% of HPMTF

530   forms OCS, resulting in the highest OCS concentration (**Figure 4i**). This stems mainly from the large contribution of the

531   photolysis reactions. Potentially, the rate constant of OH oxidation of HPMTF in KH is too low and therefore OCS might be

532   overestimated. In CS-H, 10% of HPMTF is oxidised to OCS, resulting in an OCS concentration that is on average 5.5 times

533   lower than KH. FG and WJ both use the theoretically determined branching ratio by Wu et al. (2020), which results in only

534   0.007% of HPMTF being oxidised to OCS at 295 K. NV does not include this pathway. Very recent evidence suggests that

535   there is a small (2%) but prompt source of OCS following the formation (and decomposition) of HPMTF as well as a significant

536   OCS yield (13%) from the HPMTF + OH reaction (Jernigan et al., 2022). These new data were not assessed (or included) in

537   this work but we estimate that inclusion of these mechanistic pathways would result in OCS yields higher than CS-H and the

538   other mechanisms (which have used a very small yield in the past) but consistently lower than that simulated by KH.

539   To summarise, the intercomparison of recent gas-phase DMS oxidation mechanisms complements and extends earlier studies

540   on DMS (Karl et al., 2007). Recent gas-phase DMS oxidation schemes used in modelling studies lead to a wide range in results

541   of key DMS oxidation products, with moderate Nox levels (~ 0.1 ppb) leading to greater divergence than low Nox levels (~

542   10 of ppt). A similar situation was found for isoprene by Archibald et al. (2010) and significant efforts have been employed to

543   improve our understanding of isoprene oxidation through theoretical and laboratory experiments (e.g., Jenkin et al., 2015;

544   Wennberg et al., 2018). We now focus on the role of temperature on the divergences seen thus far.

545

546   **3.2.2 Temperature dependence of different DMS-HPMTF schemes**

547   **Figure 6** shows that even though the temperature dependence of average DMS concentration is similar across all schemes, the

548   temperature dependence of average SO_2 and MSA concentration differs from scheme to scheme significantly. Most of the

549   general trends were found to be similar and in line with the trends observed for the UKCA schemes and have been explained

550   there (Section 3.1.2, **Figure 3**).

551

552   While WJ has the highest absolute change in HPMTF concentration throughout the temperature range (+131 ppt, +380%;

553   **Figure 6b**), CS-H, KH, and NV show higher relative change (+43-48 pp, +763-892%). Since FG is missing the DMS oxidation

554   by NO_3 as a potential pathway to HPMTF (via MTMP), HPMTF in FG is least affected by temperature (+34 ppt, +256%).

555

556   MSA is even more affected by temperature than HPMTF (**Figure 6c**). Its concentration shows a strong negative temperature

557   dependence in all simulations (**Figure 6c**). The magnitude of MSA-temperature dependence differs from scheme to scheme.

558   The smallest changes can be observed in NV (-47 ppt from 260 – 310 K), where only 25% of DMS that is oxidised through

559   the OH-addition pathway forms MSA. Similarly in FG (-67 ppt from 260 – 310 K), where only 40% of the OH-addition

560 pathway forms DMSO and then potentially MSA. The largest temperature dependence can be found in the KH simulation,

561 with a change of MSA concentration of -282 ppt from 260 K to 310 K, which is very similar to CS2 (**Figure 3c**).

562

563 In almost all schemes, SO_2 concentration increases with temperature (**Figure 6d**). The greatest positive change happens

564 between the atmospheric relevant temperatures 270 and 290 K. KH and CS-H show the greatest increase in this temperature

565 range with +53 ppt (+160%) and +69 ppt (+80%), respectively (WJ: +34 ppt (51%)). Starting at 295 K, SO_2 concentration

566 plateaus with further increasing temperature and even declines slightly in some simulations (Figure 6d). NV and FG are the

567 only models which show a decrease in SO_2 throughout the entire temperature range of 260 – 310 K (NV: -24 ppt, -11%, FG:

568 -22 ppt, -10%), similar to ST~CS2 in **Figure 2d**. This could be due to previously mentioned simplifications in the DMS

569 additional channel, where DMSO is either completely omitted or rapidly oxidised further.

570
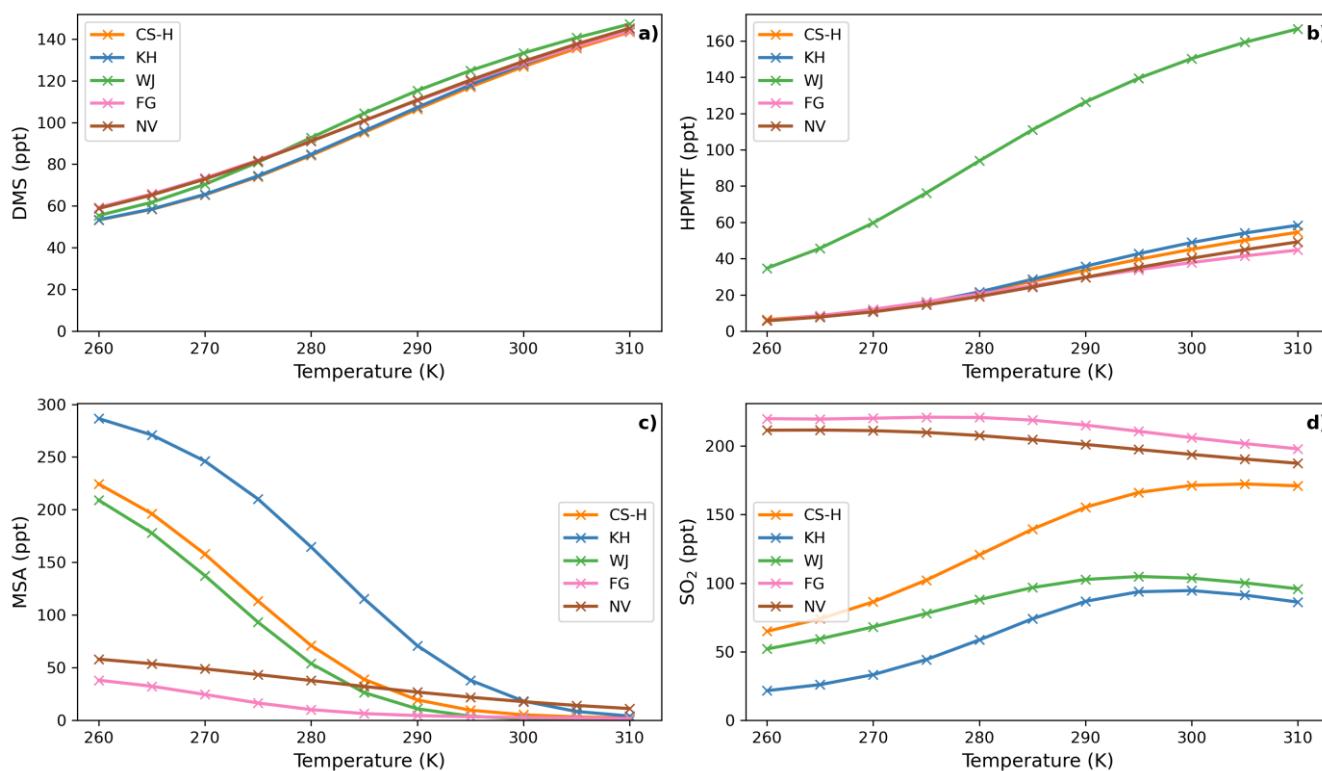
571

572 **Figure 6:** Temperature dependence of average **(a)** DMS, **(b)** HPMTF, **(c)** MSA, and **(d)** SO_2 concentration in different DMS

573 oxidation schemes after a quasi steady-state is reached in the box model simulation. Average Nox is approximately 10 ppt.

574

575 These results demonstrate limited consensus on gas-phase DMS oxidation, similar to the earlier work of Karl et al., 2007.

576 Importantly in the context of the role of DMS in chemistry-aerosol-climate feedbacks, we have further shown that this

577   uncertainty across mechanisms is amplified when assessing temperature sensitivity of the products of DMS oxidation. Small

578   uncertainties in the rate of reactions or the omission of intermediates can have significant effects on the resulting product

579   concentrations, as we have shown through our systematic work updating the CRI-Strat DMS scheme. All models studied tend

580   to agree on the rates of oxidation of DMS, largely controlled for by the fairly uniform treatment of the initial oxidation step.

581   However, we saw (in Figure 5) that there is large divergence at high Nox levels for MTMP and subsequently HPMTF and

582   SO_2. In part this divergence could be reduced by better constraining the MTMP self- and cross-reactions, but in the case of

583   Fung et al. (2022) including MTMP as a product of the NO_3 + DMS reaction would help it converge with the other models.

584   The effects of climate change are that it is likely that global mean surface temperature will remain higher than the pre-industrial

585   baseline for some time to come. As a result, the simulations would all suggest an increase in the amount of HPMTF formed

586   relative to other major oxidation products, especially, MSA, and most likely an overall increase in SO_2. However, our box-

587   modelling study highlights how uncertain the situation is within the context of the current literature. At present there is a need

588   for more laboratory data and more focused sensitivity studies to isolate the major sources of uncertainty that are common

589   across DMS oxidation mechanisms and constrain them. Strikingly we see that the ST and CS2 mechanistic variants used for

590   UKCA studies span the wide range of SO_2-Temperature and MSA-Temperature sensitivities as the recently reported updated

591   DMS mechanisms. We now move on to discuss our work implementing the CS2-H mechanism into our global chemistry-

592   climate model.

593   **4 Results from 3D model simulations using UKCA**

594   Here we present our results from the incorporation of the new CS2-H DMS mechanism described above in the 3D UKCA

595   chemistry climate model. As described in Section 2.1, we performed a series of 12-month nudged simulations with UKCA for

596   the year 2018 using 6 model simulations, with different mechanistic variants (**Table 1**). As a reminder, we use the CS2

597   simulation (Archer-Nicholls et al., 2021) as the "base" simulation, to which mechanistic improvements are made. More details

598   can be found in the SI in Section 2.

599   **4.1 Distribution of key sulfur species (DMS, HPMTF, SO_2 and sulfate).**

600   The annual mean global DMS burden was found to be between 63-66 Gg S in all model simulations. DMS concentration

601   follows a seasonal modulation with maximums in the warmer months, which coincide with phytoplankton blooms (**Fig. 7a**).

602   **Figure 7b** and **7c** show the annual mean vertical profiles in the central North Atlantic region and the Southern Ocean (see

603   figure caption for bounding areas). These regions are focused on owing to the differences shown in the mixing ratios of key

604   species and the importance of these two regions to global climate (e.g., Sutton et al., 2018; Caldeira and Duffy 2000). In the

605   Southern Ocean, DMS mixing ratios vary between 100 and >300 ppt. On the other hand, in the North Atlantic region analysed,

606   DMS concentrations rarely reach over 50 ppt. Here, <1 ppt DMS is found above the boundary layer (above 1000 m), while in

607   the Southern Ocean DMS decreases more slowly up-to the tropopause (~8000 m). These differences in DMS distribution are

608   a complex function of the local heterogeneity of the DMS source from the ocean and differences in the lifetime of DMS due

609   to different simulated cloud and oxidising environments (with the North Atlantic generally being a region of greater oxidising

610   capacity than the Southern Ocean (Archer-Nicholls et al., 2021; Griffiths et al., 2021))

611
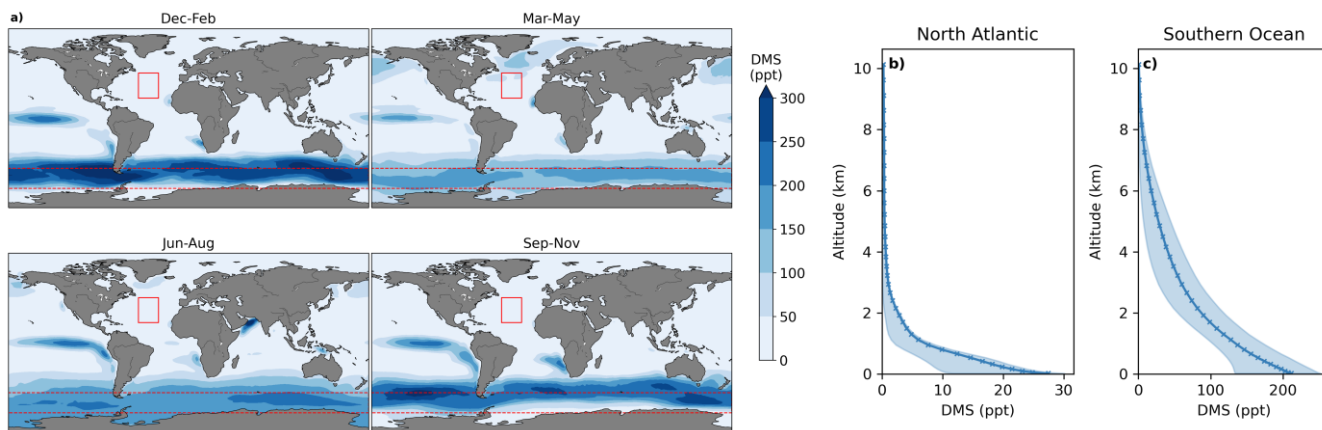
612

613   **Figure 7**: **a)** Global distribution of DMS mixing ratios in the lower troposphere (< 2 km) over the oceans in CS2. Annual mean

614   vertical distribution of DMS in **b)** the Central North Atlantic (30-50°E, 20-45°N, denoted with the red rectangle in panel **a)**

615   and in **c)** the Southern Ocean (50-70°S, denoted with the red dashed rectangle in panel **a)**. The envelopes represent the

616   interquartile range of the model simulation results. Note the order of magnitude difference in the DMS concentrations between

617   the North Atlantic and Southern Ocean.

618

619   There is a significant bias in the simulated DMS mixing ratios compared with observations, which we note has been seen in

620   several other modelling studies (e.g., Fung et al. (2022)) and is driven not by the DMS chemistry but by the oceanic emissions,

621   in our case by the bias in the UKESM derived DMS emissions field (Bhatti et al., 2023). See the SI for further details.

622

623

4.1.1 Oxidation of DMS

625   We calculate a global average tropospheric lifetime of 1.5 days for DMS. **Figure 8** shows the global distribution of the different

626   DMS oxidation pathways in the base run (these results are not affected by the different DMS mechanism variants we use as

627   these reactions were not updated and there is only a weak feedback of DMS oxidation products on DMS oxidation itself). 75%

628   of DMS is oxidised by OH (41% via the OH-addition channel and 34% via the H-abstraction channel) and 25% by NO_3.

629   Oxidation by NO_3 is dominant in the Northern Hemisphere, especially close to the coast and over ship routes. In the Southern

630   Hemisphere, where DMS emissions are highest, the contribution is less than 20%. The addition pathway of OH oxidation is

631   favoured at lower temperatures, explaining the trend of higher DMSO formation at high latitudes.

632

633
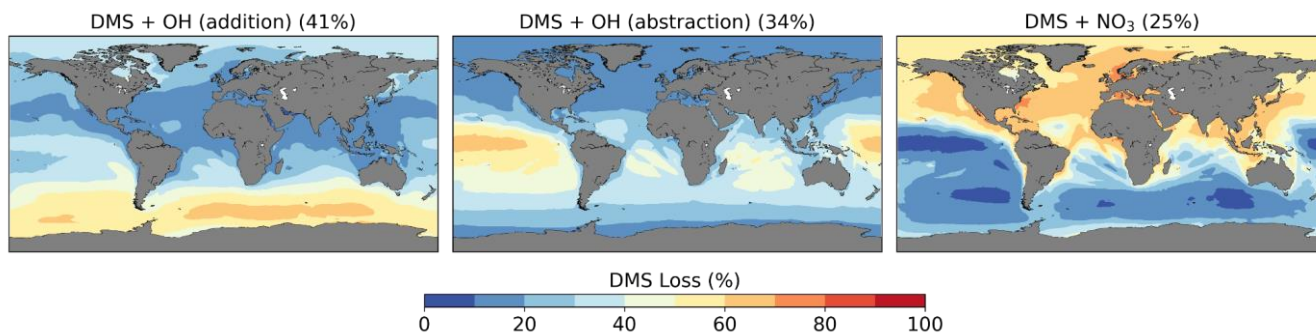
Figure 8: Spatial distribution of mean percentage of DMS oxidation via DMS + OH (addition), DMS + OH (abstraction), and DMS + NO$_3$ in the CS2 base run. The percentage in brackets denotes the contribution of this channel to the global chemical loss of DMS. Only values above the ocean are shown.

637

638

639

4.2 DMS Oxidation products

59% of DMS forms MTMP, the first intermediate of the abstraction pathway. In CS2, MTMP is oxidised by NO (51%) or reacts with itself (49%) to form CH$_3$S (**Figure 9a**) which is further oxidised to SO$_2$, H$_2$SO$_4$, and MSA. This is clearly wrong and a failure of the CS2 scheme. With the updates implemented in CS2-HPMTF, 86% of MTMP isomerizes to HPMTF, while 8% is oxidised by HO$_2$, and only 6% by NO (**Figure 9b**). The self-reaction becomes negligible with the additional loss processes of MTMP, significantly lowering MTMP concentrations. The global tropospheric lifetime of MTMP is reduced from 26 min to less than one minute.

647
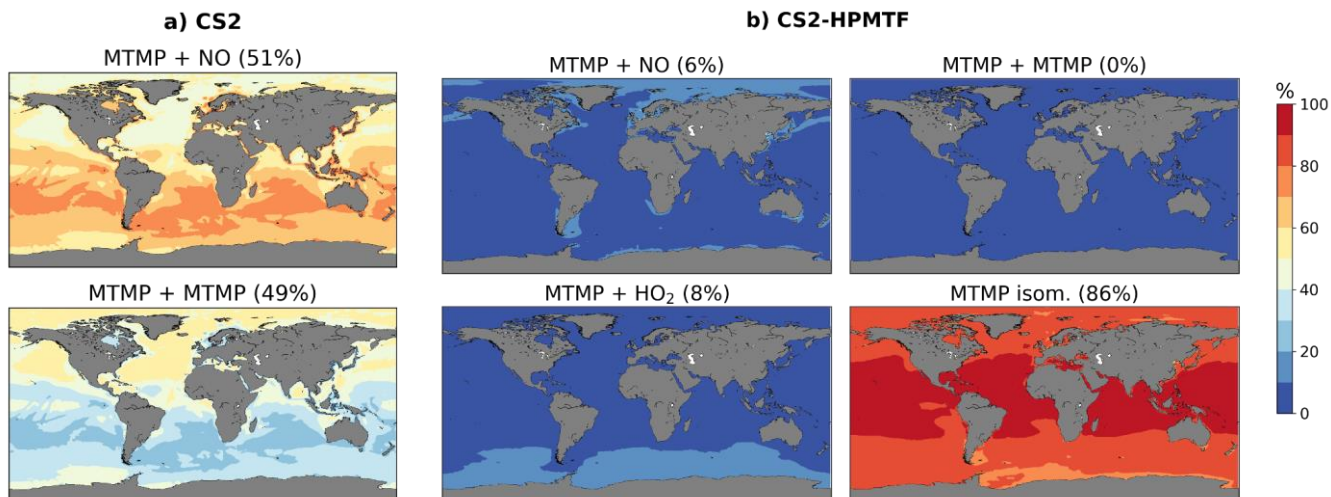
649 **Figure 9:** Spatial distribution of annual mean percentage of MTMP depletion (< 2 km) via MTMP + NO, its self-reaction,
650 MTMP + HO$_2$, and isomerization to HPMTF in **a)** CS2 and **b)** CS2-HPMTF. The percentage in brackets denotes the
651 contribution of this channel to the global chemical loss of MTMP. Only values above the ocean are shown.

4.2.1 Modelled HPMTF

In CS2-HPMTF 51% of DMS forms HPMTF. The general patterns of the global distribution of HPMTF are similar to those
of DMS in **Figure 10**, except that relatively higher concentrations of DMS are reached in the Southern Ocean. There,
temperatures are lower and therefore the OH-abstraction pathway, as well as the strongly temperature-dependent isomerization
reaction from MTMP to HPMTF are disfavoured. At the surface, the annual mean HPMTF concentration is similar in the
North Atlantic and the Southern Ocean with approximately 20 ppt. However, in the North Atlantic, the variability throughout
space and time is greater (bigger interquartile range). Further, the vertical profiles differ visibly: In the North Atlantic HPMTF
concentration decreases in the boundary layer and above 2500 m HPMTF concentration is virtually zero (**Figure 10b**). In the
Southern Ocean, the concentration decreases more slowly and only reaches zero at 10000 m (**Figure 10c**). The HPMTF burden
in CS2-HPMTF is 24 Gg S and HPMTF has a lifetime of 26 hours
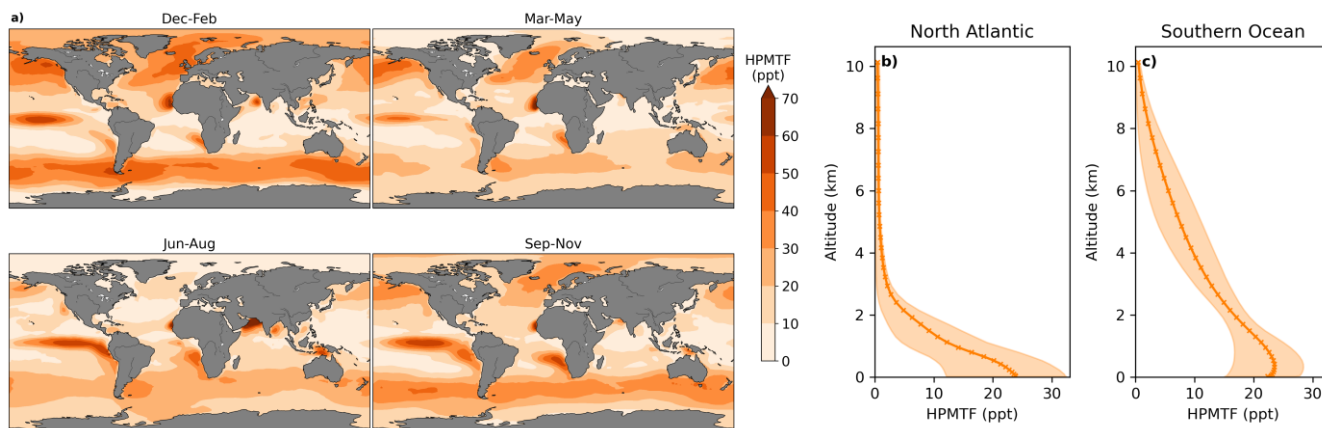
Figure 10: Seasonal average **a)** Global distribution of HPMTF mixing ratios in the lower troposphere (< 2 km) over the ocean in CS2-HPMTF. Annual means of the vertical distribution of HPMTF are shown in **b)** the Central North Atlantic (30-50°E, 20-45°N) and **c)** the Southern Ocean (50-70°S). The envelopes represent the interquartile range of the model data.

Comparison of HPMTF with observations

Since DMS in the model is likely overestimated, the same would be expected for HPMTF. **Figure 11a** shows that the implemented loss processes in CS2-HPMTF already lead to a diel profile of HPMTF that is similar to the one measured by Vermeuel et al. (2020) (where no DMS measurements were made), without the need to add aqueous loss or photolysis. While DMS at low altitudes was overestimated by a factor of 5 in the model (see SI), the maximum HPMTF is only 3.7 times higher than the highest measurement in the diel profile at Scripps Pier (**Figure 11a**). For the comparison with ATom-4 data (**Figure 11b,c**), the DMS/HPMTF is used to account for the discrepancy between DMS concentrations observed and in the model. The model generally underestimates the HPMTF/DMS ratio. For instance, up until 1000 m, the ratio in the model is half of the measured ratio. These results indicate that loss processes of HPMTF might still be too fast in the model or the oxidation of DMS too slow. The CS2 oxidants have been evaluated before (Archer-Nicholls et al., 2021) and were found to be higher in the boundary layer than in ST simulations used in CMIP6 studies but well within the spread of other models (Griffiths et al., 2021; Stevenson et al., 2020).
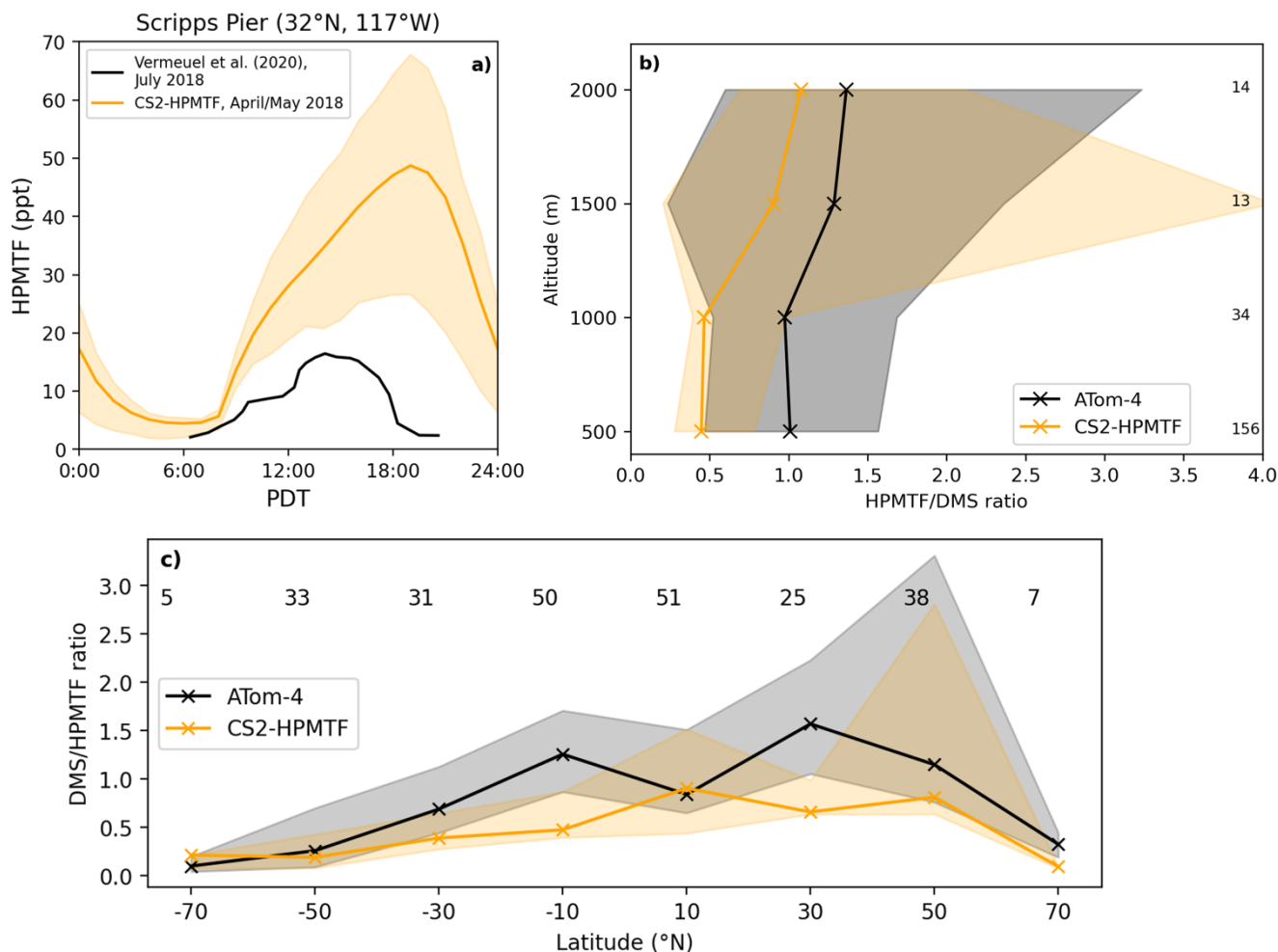
683

684 **Figure 11**: **a)** Comparison of the diel profile of HPMTF at the Scripps Pier at the California Coast (32°N, 117°W). The

685 observational data (Vermeuel et al., 2020) is the mean of measurements from July 26 to August 3, 2018, while the model

686 output is the mean from April/May 2018. **(b)** Vertically binned (500 m) and **(c)** latitudinally binned (20°) median

687 DMS/HPMTF ratio along the ATom-4 flight path. The envelopes represent the interquartile range of the measurements and

688 the respective model results while the numbers on the side/on top give the number of measurements in the respective bin.

689

690 **4.2.2 Modelled SO₂ and sulfate**

691 In CS2-HPMTF the SO$_2$ burden is increased by 5.6% compared with CS2, to 391 Gg S (**Table 4**). While this percentage seems

692 low, a significant contribution to the SO$_2$ burden stems from anthropogenic sources and is mainly located above the land. The

693 increase of SO$_2$ over the remote ocean, especially over the Southern Ocean, can reach up to 400% (**Figure 12**). At high

694   latitudes, the new chemistry implemented in CS2-HPMTF also introduces a stronger seasonality to SO_2, whereby SO_2

695   concentration is higher in respective warmer months than in CS2 (**Figure 12, Figure S10a**). Comparison of CS2-HPMTF with

696   ST reveals that the SO_2 burden is 9.2% higher in the ST run, which uses a 100% SO_2 yield from DMS (**Figure S8** in the SI).

697   The global annual tropospheric sulfate burden is increased in CS2-HPMTF by 3.7% compared with CS2, to 604 Gg S.

698   However, the sulfate burden is 5.3% higher in ST than in CS2-HPMTF (**Table 4**).

699

700
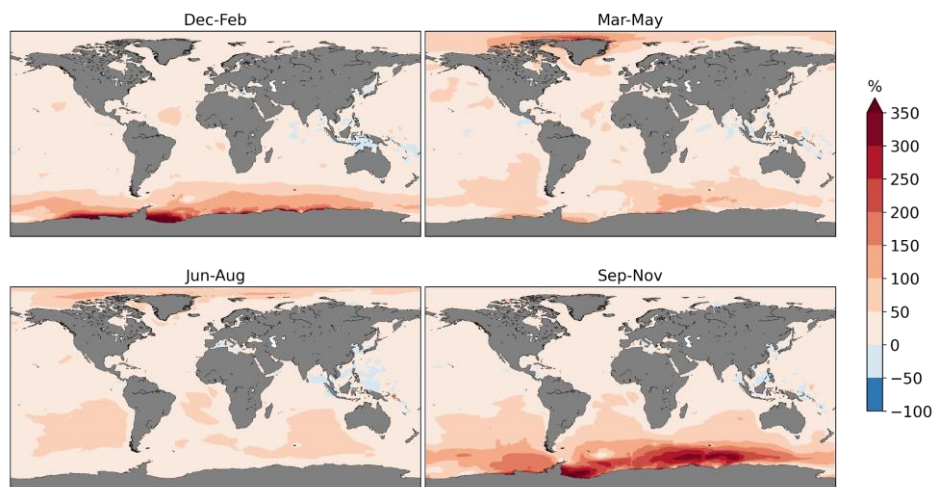
701

702   **Figure 12:** Relative difference in SO_2 mixing ratios in the lower troposphere (< 2 km) between CS2-HPMTF and the base run

703   CS2 (CS2-HPMTF - CS2). Only values above the ocean are shown.

704

705

706

707   **Comparison to observed SO_2 and sulfate**

708   **Figure 13a** shows the monthly means of observed non-sea-salt sulfate (nss-sulfate) concentration at Dumont d'Urville station

709   (66°S, 140°E) between 1991 and 1995 (Minikin et al., 1998) and compares it to the sulfate concentration in the three different

710   UKCA model runs. The seasonal changes in sulfate concentrations are reproduced by CS2-HPMTF and ST, but not by CS2.

711   From April to September all three runs match the observations adequately well. Earlier in the year, the results from the ST run

712   match the observations best, while later in the year CS2-HPMTF reproduces the measurements better.

713

714   **Figure 13b,c** show SO_2 measurements along the ATom-4 flight path in comparison with the modelled SO_2 concentrations. In

715   the boundary layer, all runs over-predict SO_2 in comparison to the ATom-4 data **(Figure 13b)**. In addition to wet and dry

716   deposition (Faloona 2009; Ranjithkumar et al., 2021), vertical mixing has been identified as a major source of uncertainty in

717   models (Gerbig et al., 2008) and could provide an explanation for the mismatch between the simulation results and

718   observations. At altitudes above 1.8 km, CS2-HPMTF is able to reflect SO_2 concentrations better than the other schemes.

719   Above 9 km, the simulations underestimate SO_2, potentially indicating issues with convective transport. Overall, in the ATom-

720   4 observations, SO_2 stays broadly constant with altitude, suggesting significant secondary sources or efficient vertical transport,

721   while in the simulations it decreases. Additionally, the interquartile ranges of the concentrations in each bin are bigger,

722   indicating a greater variance of model results than measured values. Overall, the mean SO_2 concentrations by the models in

723   each latitude bin predict the mean observation values well (**Figure 13c**). However, the variation of values is again greater in

724   the model, especially at low latitudes. The underestimation of SO_2 at 70°N could be due to an underestimation of the influence

725   of anthropogenic SO_2 emissions or unrealistic deposition of SO_2 (Hardacre et al., 2021). Alternatively, the SO_2 production

726   from DMS might be too slow still.

727

728
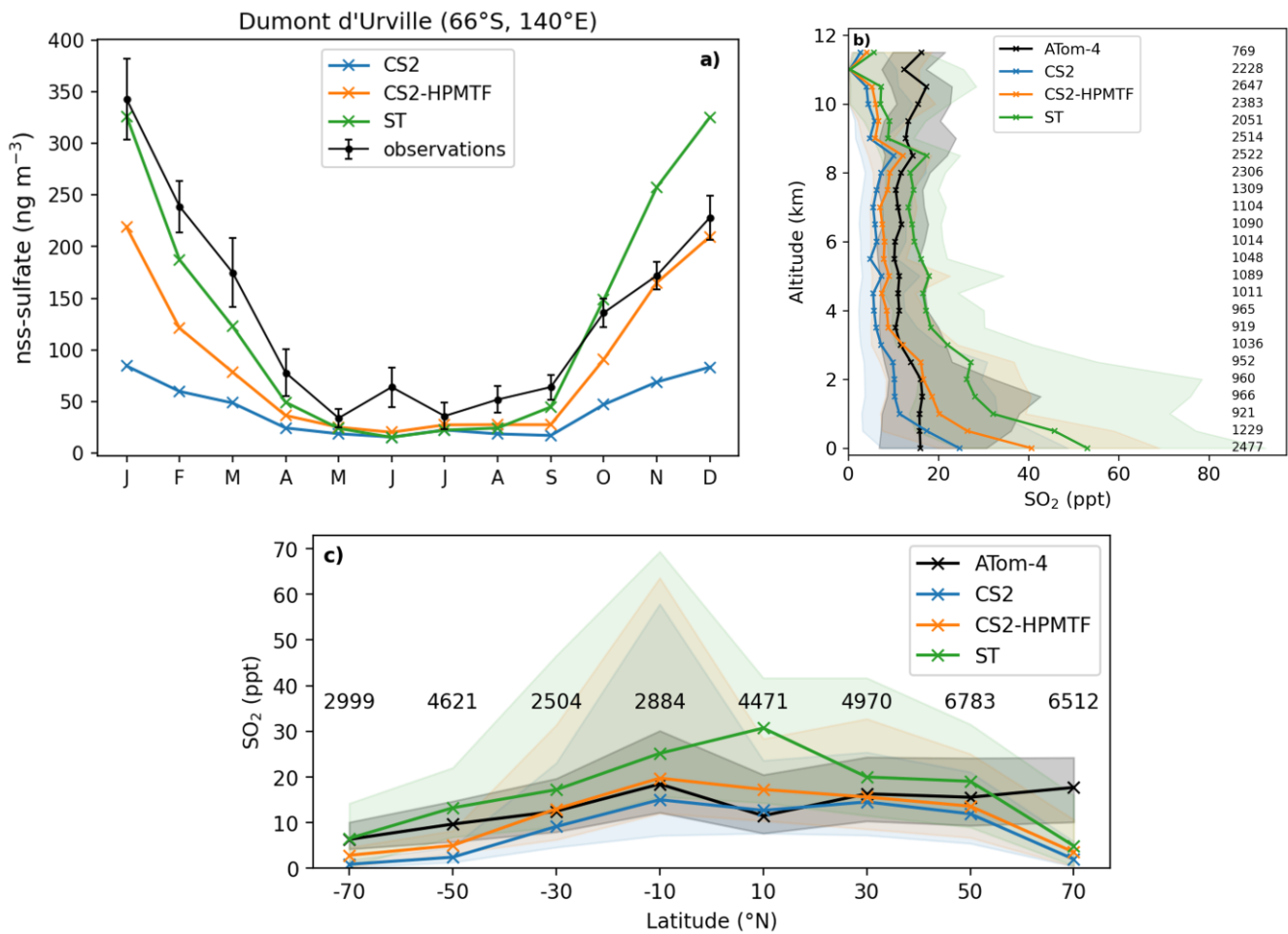
729

730 **Figure 13: a)** Comparison of nss-sulfate concentration at the Dumont d'Urville Station (66°S, 140°E) at the coast of Antarctica.

731 The observational data stems from Minikin et al. (1998) and represents the monthly mean concentrations and their standard

732 deviations for the years 1991-1995. **(b)** Vertically binned (500 m) and **(c)** latitudinally binned (20°) median SO_2 mixing ratio

733 along the ATom-4 flight path. The envelopes represent the interquartile range of the measurements and the respective model

734 results while the numbers on the side/on top give the number of measurements in the respective bin.

735

736

737 ### 4.3 Sensitivity runs

738 To improve our understanding of the variability of the model results, based on the uncertainties of HPMTF formation and loss,

739 three sensitivity runs were conducted (CS2-HPMTF-CLD, CS2-HPMTF-FL, CS2-HPMTF-FP, **Table 1**). Loss of HPMTF to

740 clouds was proposed to be a major loss pathway by Veres et al. (2020) and Vermeuel et al. (2020). CS2-HPMTF-CLD adds

741 cloud and aqueous uptake of HPMTF with a reactive uptake coefficient, γ, of 0.01, used in the study by Novak et al. (2021).

742 Jernigan et al. (2022) recently established a rate constant for oxidation of HPMTF by OH as 1.4 (0.27–2.4) $\times 10^{-11}$ cm^3 molecule^{-1}

743 ^{1} s^{-1} through constrained chamber modelling using a rate constant for the formation of HPMTF as 0.1 s^{-1}. Ye et al. (2022) also

744 measured the rate constant for this reaction. In their study they derived a rate constant of 2.1×10^{-11} cm^3 molecule^{-1} s^{-1} and an

745 isomerization rate constant, k_{isom}, of 0.13±0.03 s^{-1} at 295 K. Whilst, further laboratory studies would be helpful in constraining

746 the rate constant for OH + HPMTF, we recommend future work go into constraining the products of this reaction. Vermeuel

747 et al. (2020) found the theoretically calculated rate constant 1.4×10^{-12} cm^3 molecule^{-1} s^{-1} by Wu et al. (2015) too slow and

748 proposed a rate constant of 1.11×10^{-11} cm^3 molecule^{-1} s^{-1} instead, based on structurally similar molecules and modelling of their

749 ground-based observations, similar to what we used in CS2-HPMTF. They recommend an upper limit of 5.1×10^{-11} cm^3

750 molecule^{-1} s^{-1} for the HPMTF+OH rate constant. Khan et al. (2021) and Novak et al. (2021) use 5.5×10^{-11} cm^3 molecule^{-1} s^{-1} for

751 sensitivity tests, which was also employed in CS2-HPMTF-FL. Further, the study by Ye et al. (2021) looked at the uncertainty

752 of the HPMTF isomerization rate. They estimate the isomerization rate constant as 0.09 s^{-1} (0.03-0.3 s^{-1}, 1σ$_g$ geometric standard

753 deviation at 293 K). Veres et al. (2020) are on the lower end of this range (0.041 s^{-1}) and Berndt et al. (2019) at the higher end

754 (0.23 s^{-1}). The CS2-HPMTF-FP simulation scales the rate constant of Veres et al. (2020) by a factor of 5 to match Berndt's

755 measurements at 295 K to examine the effects of higher HPMTF production. This rate constant was also used by Wollesen de

756 Jonge et al. (2021) in their study. The annual mean of global tropospheric burdens of relevant species in these sensitivity runs

757 are compared in **Table 4.**

758

759 **Table 4:** Global annual mean tropospheric burdens of atmospheric sulfur species in UKCA base and sensitivity runs (first half

760 of the table) and comparison to literature values (second half of the table, same acronyms as in Section 3)

Run	HPMTF burden (Gg S)	SO_2 burden (Gg S)	Sulfate burden (Gg S)

CS2	-	370.1	582.3
ST	-	469.7	635.9
CS2-HPMTF	23.7	390.7	604.0
CS2-HPMTF-CLD	2.6	367.3	591.2
CS2-HPMTF-FL	8.9	392.6	605.6
CS2-HPMTF-FP	26.5	389.6	601.5
FG[⊗] (similar to CS2-HPMTF)	18	365	582
NV Base 1[⊕] (similar to CS2-HPMTF)	18.8	189.0	526.7
NV Test 3[⊕] (similar to CS2-HPMTF-CLD)	0.7	180.2	550.7
KH NEW_CHEM1[⊘] (similar to CS2-HPMTF, with photolysis of HPMTF)	15.1	-	-
KH NEW_CHEM2[⊘] (similar to CS2-HPMTF-FL)	6.1	-	-

[⊗]Fung et al., 2021; [⊕]Novak et al., 2021; [⊘] Khan et al., 2021.

4.3.1 HPMTF

The HPMTF burden varies between 2.6 and 26.5 Gg S among the sensitivity runs (**Table 4**). Compared to CS2-HPMTF, faster OH oxidation reduces the HPMTF burden by -62% to 8.9 Gg S, while the addition of cloud and aqueous uptake to the scheme reduces it by -91% to only 2.6 Gg S. Yet, a factor of 5 higher production rate constant of HPMTF only leads to a 12% increase of HPMTF burden to 26.5 Gg S; suggesting that the steady-state distribution of HPMTF is controlled by the loss rate, not the rate of production of HPMTF. With the isomerization rate constant recommended by Veres et al. (2020), 51% of DMS forms HPMTF (86% of MTMP); with the faster rate in CS2-HPMTF-FP it is 57% (96% of MTMP). Since the use of the isomerization rate from Veres et al. (2020) already outcompetes the bimolecular reactions of MTMP, scaling the A-factor does not have a significant effect on the HPMTF yield from DMS. Overall, it can be estimated that globally 50-60% of DMS forms HPMTF (however, if more DMS is oxidised through the addition channel by BrO or multiphase reactions, this ratio could be lower). Consequently, HPMTF formation seems to be well constrained and the major uncertainties lie with the loss of HPMTF, which warrant additional measurements.

Similar to **Figure 11**, the HPMTF:DMS ratio is used in **Figure 14** to compare the results of the sensitivity model runs with ATom-4 observations. In general, schemes with a higher production and slower loss of HPMTF match the observations better, however, they still underestimate the measured ratios. A comparison was made to HPMTF:DMS ratios measured with no clouds present. Under these clear-sky conditions, when cloud uptake of HPMTF should not play a role in the measurements, observed ratios were even higher, leading to a greater difference between model results (which include clouds) and observations.
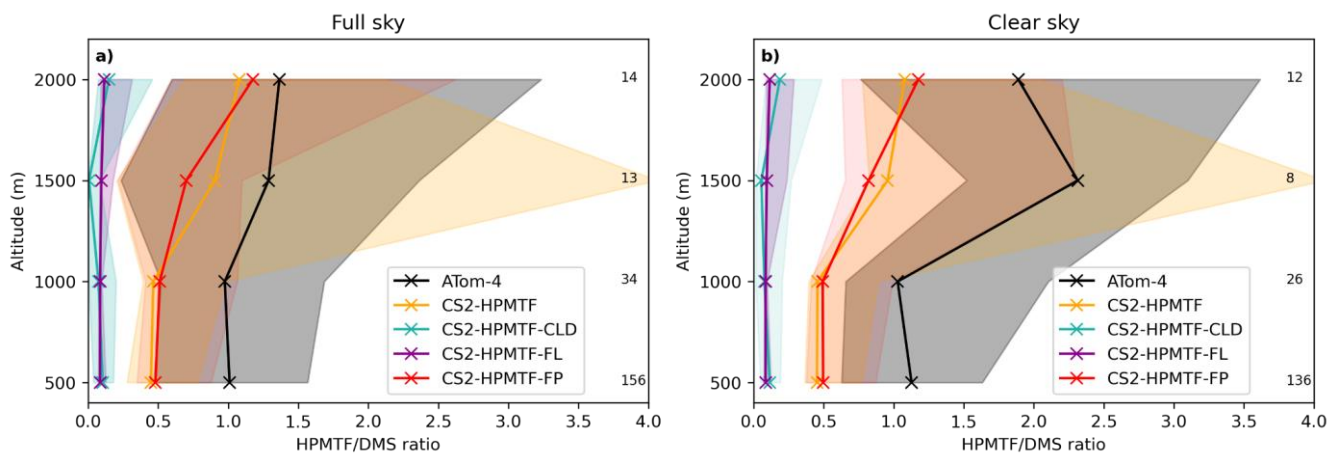
782

783 **Figure 14:** Vertically binned (500 m) median HPMTF/DMS ratio along the ATom-4 flight path for **a)** full sky and **b)** clear
784 sky, where measurements made in clouds are omitted. The envelopes represent the interquartile range of the measurements
785 and the respective model results, while values on the side give the number of measurements in the respective bin. Note that
786 the model data is the same in both panels.

787

788 **4.3.2 SO$_2$**

789 The SO$_2$ burden varies between 367.3 Gg S in CS2-HPMTF-CLD and 392.6 GgS in CS2-HPMTF-FL, suggesting that the SO$_2$
790 burden is relatively unaffected by the chemical sensitives explored when compared with the much larger SO$_2$ burden simulated
791 with ST (469.7 Gg S); mainly due to the 100% DMS-SO$_2$ yield (**Table 4**).

792

793 CS2-HPMTF, CS2-HPMTF-FL, and CS2-HPMTF-FP have a higher SO$_2$ burden than CS2 since the changes to the abstraction
794 pathway (reaction 6a, 7c) and the addition of the isomerization pathway lead to more direct SO$_2$ production. Faster OH
795 oxidation of HPMTF in CS2-HPMTF-FL reduces the amount of HPMTF deposited and therefore increases the SO$_2$ burden
796 slightly (by 0.5%) compared to CS2-HPMTF. The faster production of HPMTF in CS2-HPMTF-FP reduces SO$_2$ burden
797 marginally (-0.3%), due to more sulfur now being deposited as HPMTF or forming OCS. The addition of cloud and
798 heterogeneous loss in CS2-HPMTF-CLD leads to immediate sulfate production instead of SO$_2$ formation, reducing the SO$_2$
799 burden by -6% compared to CS2-HPMTF, resulting in the lowest SO$_2$ burden in all runs considered.

800

801 **4.4.3 Sulfate**

802 In the sensitivity runs, the sulfate burdens are all higher than in the CS2 run (582.3 Gg S) and lower than in the ST run (635.9
803 Gg S). The variation by approximately 15 Gg S, from 591.2 Gg S in CS2-HPMTF-CLD to 605.6 Gg S in CS2-HPMTF-FL, is

804   smaller than the variation in sulfate burden simulated by similar mechanistic sensitivity tests by Novak et al. (2021) (~24 Gg),

805   suggesting some structural dependence on the results of the sensitivity tests (e.g., resolution, other model parameters). The

806   sulfate burdens in CS2-HPMTF-FL and CS2-HPMTF-FP behave similarly to CS2-HPMTF. Since CS2-HPMTF-CLD added

807   direct sulfate formation, a higher sulfate burden was expected. However, this was not seen in the experiments. Inspection of

808   the sulfate aerosol distribution shows that CS2-HPMTF-CLD leads to an increase in the coarse mode sulfate and a concomitant

809   reduction in sulfate aerosol lifetime (through an increase in wet deposition).

810

811

5 Discussion

813   The results described above demonstrate the global scale changes in the distribution of DMS and its oxidation products, through

814   the incorporation of improved mechanistic updates into the UKCA model. Here we discuss our results in the context of the

815   existing literature.

5.1 DMS

817   The DMS burden of 63-66 Gg S in this work is in good agreement with recent modelling studies (50 Gg S in Fung et al. (2022),

818   74 Gg S in Chen et al. (2018)). However, as shown in the supplement, S2.1.1, the modelled DMS concentrations do not match

819   observational measurements. One explanation could be underestimation of DMS oxidation. Here, only oxidation by OH and

820   NO_3 is included. However, Fung et al. (2022), who include oxidation by BrO, O_3 and Cl (accounting in total for 20% of DMS

821   depletion), also found that their model over-predicted DMS mixing ratios compared to the ATom-4 measurements. Inadequate

822   representation of DMS concentrations in seawater and therefore emissions contribute to the largest uncertainties in the sulfur

823   budget (Tesdal et al., 2016; Bock et al., 2021) and could explain most of the difference. Additionally, physical differences

824   between model and observation, such as wind speed and temperature, and a poor space resolution of Whole Air Sampling

825   might also play a role. Crucially, more long-term observations of DMS in the atmosphere are needed to complement works

826   that have collated oceanic DMS observations (e.g., Lana et al., 2011).

827

828   Here, in all model runs 75% of DMS is oxidised by OH and 25% by NO_3. Other studies found global contributions of OH

829   between 50-70% and NO_3 15-30% (Boucher et al., 2003; Berglen et al., 2004; Breider et al., 2010; Khan et al., 2016; Chen et

830   al., 2018; Fung et al., 2022). The lower contribution of OH oxidation to DMS removal is explained by the addition of other

831   pathways, such as oxidation by BrO, Cl and multiphase reactions. Consequently, the lifetime of 1.5 days for DMS in this work

832   is longer than some other studies including these reactions (e.g., 0.8 days in Fung et al. (2022) and 1.2 days in Chen et al.

833   (2018)). Nonetheless, it is well within the range of 0.9 to 5 days (with a mean of 2 days) of the models examined in Faloona

834   (2009).

835

836

5.2 HPMTF

In CS2-HPMTF 51% of DMS forms HPMTF. With a faster formation of HPMTF, found in laboratory experiments, this yield increases to 57% in our model. The yield could possibly be lower if other oxidation reactions of DMS are included that follow the OH addition pathway (multiphase reactions, oxidation by BrO), which was omitted in this work. Veres et al. (2020), Novak et al. (2021) and Fung et al. (2022) estimated that at least 30-46% of DMS was forming HPMTF, based on observationally constrained modelling of *in situ* or laboratory data. Even though the rate of HPMTF formation is uncertain (Ye et al., 2021), it does not significantly affect the HPMTF yield from DMS, since it already outcompetes most other reactions of MTMP. For HPMTF formation, uncertainty seems to lie mainly at the branching ratio of the addition and the abstraction pathway of DMS. Indeed, the uncertainty in the HPMTF burden stems from the uncertainty in the loss pathways and their respective contribution to HPMTF loss. Our model results agree well with the HPMTF burdens obtained by other global modelling studies, both in absolute values but also the relative changes we find in the sensitivity study (**Table 4**) (e.g., Fung et al. (2022)): In our sensitivity study a faster oxidation of HPMTF to OH lead to a decrease of 62% of the HPMTF burden, in Khan et al. (2021) it was 60%. In this work the addition of aqueous uptake of HPMTF reduced the burden by 91%, very similar to the reduction simulated in Novak et al. (2021) (96%).

851

5.3 MSA

The tropospheric MSA burden is 40 Gg S in CS2-HPMTF with a lifetime of 6 days. This falls within the range of 13-40 Gg S and a lifetime of 5-7 days found in previous model studies (Pham et al., 1995; Chin et al., 1996, 2000; Cosme et al., 2002; Hezel et al., 2011). However, newer studies include more multiphase processes and usually tend to have shorter lifetimes and lower MSA burdens. Both the scheme in Fung et al. (2022) and Chen et al. (2018), include the loss of MSA to aqueous OH oxidation, resulting in lifetimes of 0.6 days and 2.2 days and a burden of 8 Gg S and 20 Gg S, respectively.

5.4 SO_2 and Sulfate

Comparing SO_2 and sulfate burdens with other modelling studies is more challenging, since those species can have other sources apart from DMS. That said, our SO_2 obtained in the various runs based on the CS2 scheme are comparable to Fung et al. (2022), while the ST burden is significantly higher. However, the SO_2 burden from Novak et al. (2021) is much lower. This difference cannot be explained solely by differences in the DMS oxidation mechanism; more likely, the difference is in anthropogenic SO_2 emissions.

The sulfate burden in all our runs fall within the range found in other recent modelling studies (Chen et al. 2018; Novak et al., 2021; Fung et al., 2022). Considering the relative change due to the addition of the isomerization pathway, the increase in sulfate burden from CS2 to CS2-HPMTF is only 3.7% in our study, Fung et al. (2022) found an increase of 8.8%, when they

867 added HPMTF chemistry. However, unlike their results, we find strong seasonality in the additional sulfate produced,
868 especially in the Southern Hemisphere. The addition of cloud uptake and direct sulfate formation in CS2-HPMTF-CLD
869 decreased the sulfate burden in our study by (-)2.2%, in Novak et al. (2021) this change in mechanism lead to an increase of
870 sulfate by 4.5%.

871

872 **5.5 Comparison with BOXMOX results.**

873 In Section 3 and Section 4 we have shown the results of BOXMOX and UKCA simulations using different DMS mechanistic
874 variants respectively. Whilst the same mechanistic variants have been assessed in both model setups, it is not possible to
875 directly compare the results of the two sets of experiments because of the large differences in the model setups used. However,
876 some qualitative comparisons can be made. For MSA, Section 3.1 (Figure 2) suggests that the MSA simulated with CS2-
877 HPMTF should be much lower than CS2; as is calculated in Section 4.2.2 (a 70% reduction). For SO_2, both the BOXMOX
878 and UKCA results agree in the ordering of simulations, ST, CS2 and CS2-HPMTF; with ST simulating significantly more SO_2
879 than the other mechanisms. However, whereas BOXMOX simulations suggest that H_2SO_4 is predicted to be higher in CS2 and
880 CS2-HPMTF than ST, the UKCA model runs suggest that ST has the greatest burden of sulfate; highlighting the complexity
881 of making inference on aerosols from gas phase precursors in box model studies.

882

883 **6 Conclusion**

884 DMS remains an important molecule in our understanding of the background aerosol budget and the uncertainty of aerosols
885 to climate change (Carslaw et al., 2013). In this study we have used a combination of box modelling experiments and global
886 3D model experiments to explore the sensitivities of the DMS oxidation mechanism in the UKCA model. This work has
887 delivered a new DMS oxidation mechanism for use within the CRI-Strat framework of UKCA (Archer-Nicholls et al., 2021;
888 Weber et al., 2021), which is a significant advancement and improvement over the mechanism used in CMIP6 studies
889 (Archibald et al., 2020). Our new DMS mechanism includes many of the recently discovered and proposed oxidation pathways
890 for DMS and through the series of experiments we have performed, we have been able to benchmark this scheme against other
891 recently reported schemes in the literature. Whilst future studies building on the ever expanding database of laboratory studies
892 (e.g., Ye et al., 2021; Jernigan et al., 2022) are required to refine the DMS oxidation mechanism further, with the current
893 availability of observational data, it is not possible to fully constrain the uncertain parameters in the DMS oxidation
894 mechanism. Hence there is a priority for more observational based studies that combine ship, ground-based and aircraft
895 platforms optimally. Fung et al. (2021) have shown that there are consequences for radiative forcing by updating the DMS
896 mechanism in the CESM model, and follow up work will investigate these changes with UKCA.

897

898 This study adds to the few other mechanism intercomparisons that exist in the literature, spanning back more than 25 years
899 (Capaldo and Pandis 1997; Karl et al., 2007). Similar to these other studies we find that MSA is particularly uncertain when it
900 comes to the results obtained using the range of mechanisms that we investigated. Further work should explicitly focus on
901 reducing uncertainty in the MSA budget in the atmosphere, especially given its potential importance in reconstructing paleo-
902 sea ice (Thomas et al., 2019).

903

904 In many ways, the recent advances in DMS oxidation chemistry are similar to isoprene chemistry, where over a decade ago
905 the discovery of uni-molecular isomerisation reactions resulted in a step-change in our understanding of isoprene. As with
906 isoprene, ever more complex and faithful descriptions of DMS chemistry will be delivered over the coming years. But the
907 biggest challenge (as for isoprene) will remain in reducing and accurately distilling down this complex chemistry for use in
908 global model studies, and in characterising the sources of DMS into the atmosphere (which for isoprene have only recently
909 been possibly directly e.g., Wells et al., 2020).

910

911 **Acknowledgements**

912 BAC thanks the Studienstiftung des Deutschen Volkes for financial support. We would like to thank NERC through the ACSIS
913 (NE/N018001/1) and CARES projects for funding (NE/W009412/1). We would like to thank the UK Met Office JWCRP and
914 Clean Air programmes and the National Centre for Atmospheric Science for funding the development of the UKCA model.
915 LER acknowledges support from the Deep South National Science Challenge (contract C01X1901). ATA thanks the
916 University of Canterbury Erskine Programme. This work used Monsoon2, a collaborative high-performance computing facility
917 funded by the Met Office and the Natural Environment Research Council. This work used JASMIN, the UK collaborative data
918 analysis facility.

919
920 **Competing interests**
921 The authors declare no competing interests.

References

Assaf, E., Finewax, Z., Marshall, P., Veres, P.R., Neuman, J.A. and Burkholder, J.B.: Measurement of the Intramolecular Hydrogen-Shift Rate Coefficient for the CH3SCH2OO Radical between 314 and 433 K. *The Journal of Physical Chemistry A*, *127*(10), pp.2336-2350, 2023.

Andreae, M. O.: Ocean-atmosphere interactions in the global biogeochemical sulfur cycle, Marine Chemistry, 30, 1–29, https://doi.org/10.1016/0304-4203(90)90059-L, 1990.

Archer-Nicholls, S., Abraham, N. L., Shin, Y. M., Weber, J., Russo, M. R., Lowe, D., Utembe, S. R., O'Connor, F. M., Kerridge, B., Latter, B., Siddans, R., Jenkin, M., Wild, O., and Archibald, A. T.: The Common Representative Intermediates Mechanism Version 2 in the United Kingdom Chemistry and Aerosols Model, 13, e2020MS002420, https://doi.org/10.1029/2020MS002420, 2021.

Archibald, A. T., Jenkin, M. E., and Shallcross, D. E.: An isoprene mechanism intercomparison, Atmospheric Environment, 44, 5356–5364, https://doi.org/10.1016/j.atmosenv.2009.09.016, 2010.

Archibald, A. T., O'Connor, F. M., Abraham, N. L., Archer-Nicholls, S., Chipperfield, M. P., Dalvi, M., Folberth, G. A., Dennison, F., Dhomse, S. S., Griffiths, P. T., Hardacre, C., Hewitt, A. J., Hill, R. S., Johnson, C. E., Keeble, J., Köhler, M. O., Morgenstern, O., Mulcahy, J. P., Ordóñez, C., Pope, R. J., Rumbold, S. T., Russo, M. R., Savage, N. H., Sellar, A., Stringer, M., Turnock, S. T., Wild, O., and Zeng, G.: Description and evaluation of the UKCA stratosphere–troposphere chemistry scheme (StratTrop vn 1.0) implemented in UKESM1, 13, 1223–1266, https://doi.org/10.5194/gmd-13-1223-2020, 2020.

Arsene, C., Barnes, I., and Becker, K. H.: FT-IR product study of the photo-oxidation of dimethyl sulfide: Temperature and O_2 partial pressure dependence, Phys. Chem. Chem. Phys., 1, 5463–5470, https://doi.org/10.1039/A907211J, 1999.

Atkinson, R., Baulch, D. L., Cox, R. A., Crowley, J. N., Hampson, R. F., Hynes, R. G., Jenkin, M. E., Rossi, M. J., and Troe, J.: Evaluated kinetic and photochemical data for atmospheric chemistry: Volume I - gas phase reactions of O_x, HO_x, NO_x and SO_x species, 4, 1461–1738, https://doi.org/10.5194/acp-4-1461-2004, 2004.

Barnes, I., Hjorth, J., and Mihalopoulos, N.: Dimethyl Sulfide and Dimethyl Sulfoxide and Their Oxidation in the Atmosphere, Chem. Rev., 106, 940–975, https://doi.org/10.1021/cr020529+, 2006.

Barone, S., A. Turnipseed, A., and R. Ravishankara, A.: Role of adducts in the atmospheric oxidation of dimethyl sulfide, 100, 39–54, https://doi.org/10.1039/FD9950000039, 1995.

Berglen, T. F., Berntsen, T. K., Isaksen, I. S. A., and Sundet, J. K.: A global model of the coupled sulfur/oxidant chemistry in the troposphere: The sulfur cycle, 109, https://doi.org/10.1029/2003JD003948, 2004.

950 Berndt, T., Scholz, W., Mentler, B., Fischer, L., Hoffmann, E. H., Tilgner, A., Hyttinen, N., Prisle, N. L., Hansel, A., and
951 Herrmann, H.: Fast Peroxy Radical Isomerization and OH Recycling in the Reaction of OH Radicals with Dimethyl Sulfide,
952 J. Phys. Chem. Lett., 10, 6478–6483, https://doi.org/10.1021/acs.jpclett.9b02567, 2019.

953 Bhatti, Y., Revell, L., Schuddeboom, A., McDonald, A., Archibald, A., Williams, J., Venugopal, A., Hardacre, C., and
954 Behrens, E.: The sensitivity of Southern Ocean atmospheric dimethyl sulfide to modelled sources and emissions, EGUsphere
955 [preprint], https://doi.org/10.5194/egusphere-2023-868, 2023.

956 Bock, J., Michou, M., Nabat, P., Abe, M., Mulcahy, J. P., Olivié, D. J. L., Schwinger, J., Suntharalingam, P., Tjiputra, J., van
957 Hulten, M., Watanabe, M., Yool, A., and Séférian, R.: Evaluation of ocean dimethylsulfide concentration and emission in
958 CMIP6 models, 18, 3823–3860, https://doi.org/10.5194/bg-18-3823-2021, 2021.

959 Borissenko, D., Kukui, A., Laverdet, G., and Le Bras, G.: Experimental Study of SO2 Formation in the Reactions of CH3SO
960 Radical with NO2 and O3 in Relation with the Atmospheric Oxidation Mechanism of Dimethyl Sulfide, J. Phys. Chem. A,
961 107, 1155–1161, https://doi.org/10.1021/jp021701g, 2003.

962 Boucher, O., Moulin, C., Belviso, S., Aumont, O., Bopp, L., Cosme, E., von Kuhlmann, R., Lawrence, M. G., Pham, M.,
963 Reddy, M. S., Sciare, J., and Venkataraman, C.: DMS atmospheric concentrations and sulphate aerosol indirect radiative
964 forcing: a sensitivity study to the DMS source representation and oxidation, 3, 49–65, https://doi.org/10.5194/acp-3-49-2003,
965 2003.

966 Breider, T. J., Chipperfield, M. P., Richards, N. a. D., Carslaw, K. S., Mann, G. W., and Spracklen, D. V.: Impact of BrO on
967 dimethylsulfide in the remote marine boundary layer, 37, https://doi.org/10.1029/2009GL040868, 2010.

968 de Bruyn, W. J., Harvey, M., Cainey, J. M., and Saltzman, E. S.: DMS and SO2 at Baring Head, New Zealand: Implications
969 for the Yield of SO2 from DMS, Journal of Atmospheric Chemistry, 41, 189–209, https://doi.org/10.1023/A:1014252106572,
970 2002.

971 Butkovskaya, N. I. and Barnes, I.: Model Study of the Photooxidation of CH3SO2SCH3 at Atmospheric Pressure: Thermal
972 Decomposition of the CH3SO2 Radical, in: Global Atmospheric Change and its Impact on Regional Air Quality, edited by:
973 Barnes, I., Springer Netherlands, Dordrecht, 147–152, https://doi.org/10.1007/978-94-010-0082-6_22, 2002.

974 Butkovskaya, N. I. and LeBras, G.: Mechanism of the NO3 + DMS Reaction by Discharge Flow Mass Spectrometry, J. Phys.
975 Chem., 98, 2582–2591, https://doi.org/10.1021/j100061a014, 1994.

976 Caldeira, K. and Duffy, P.B. The role of the Southern Ocean in uptake and storage of anthropogenic carbon dioxide. Science,
977 287(5453), pp.620-622. 2000.

978 Campolongo, F., Saltelli, A., Jensen, N. R., Wilson, J., and Hjorth, J.: The Role of Multiphase Chemistry in the Oxidation of
979 Dimethylsulphide (DMS). A Latitude Dependent Analysis, Journal of Atmospheric Chemistry, 32, 327–356,
980 https://doi.org/10.1023/A:1006154618511, 1999.

981 Cao, J., Wang, W.L., Gao, L.J. and Fu, F.: Mechanism and thermodynamic properties of CH_3SO_3 decomposition. Acta
982 Physico-Chimica Sinica, 29(6), 1161-1167, https://doi.org/10.3866/PKU.WHXB201304021, 2013.

983 Capaldo, K.P. and Pandis, S.N. Dimethylsulfide chemistry in the remote marine atmosphere: Evaluation and sensitivity
984 analysis of available mechanisms. Journal of Geophysical Research: Atmospheres, 102(D19), pp.23251-23267. 1997

985

986 Carslaw, K. S., Lee, L. A., Reddington, C. L., Pringle, K. J., Rap, A., Forster, P. M., Mann, G. W., Spracklen, D. V.,
987 Woodhouse, M. T., Regayre, L. A., and Pierce, J. R.: Large contribution of natural aerosols to uncertainty in indirect forcing,
988 503, 67–71, https://doi.org/10.1038/nature12674, 2013.

989 Charlson, R. J., Lovelock, J. E., Andreae, M. O., and Warren, S. G.: Oceanic phytoplankton, atmospheric sulphur, cloud albedo
990 and climate, 326, 655–661, https://doi.org/10.1038/326655a0, 1987.

991 Chen, H. and Finlayson-Pitts, B. J.: New Particle Formation from Methanesulfonic Acid and Amines/Ammonia as a Function
992 of Temperature, Environ. Sci. Technol., 51, 243–252, https://doi.org/10.1021/acs.est.6b04173, 2017.

993 Chen, H., Ezell, M. J., Arquero, K. D., Varner, M. E., Dawson, M. L., Gerber, R. B., and Finlayson-Pitts, B. J.: New particle
994 formation and growth from methanesulfonic acid, trimethylamine and water, Phys. Chem. Chem. Phys., 17, 13699–13709,
995 https://doi.org/10.1039/C5CP00838G, 2015.

996 Chen, J., Berndt, T., Møller, K. H., Lane, J. R., and Kjaergaard, H. G.: Atmospheric Fate of the CH3SOO Radical from the
997 CH3S + O2 Equilibrium, J. Phys. Chem. A, 125, 8933–8941, https://doi.org/10.1021/acs.jpca.1c06900, 2021.

998 Chen, Q., Sherwen, T., Evans, M., and Alexander, B.: DMS oxidation and sulfur aerosol formation in the marine troposphere:
999 a focus on reactive halogen and multiphase chemistry, 18, 13617–13637, https://doi.org/10.5194/acp-18-13617-2018, 2018.

1000 Chin, M., Jacob, D. J., Gardner, G. M., Foreman-Fowler, M. S., Spiro, P. A., and Savoie, D. L.: A global three-dimensional
1001 model of tropospheric sulfate, 101, 18667–18690, https://doi.org/10.1029/96JD01221, 1996.

1002 Chin, M., Savoie, D. L., Huebert, B. J., Bandy, A. R., Thornton, D. C., Bates, T. S., Quinn, P. K., Saltzman, E. S., and Bruyn,
1003 W. J. D.: Atmospheric sulfur cycle simulated in the global model GOCART: Comparison with field observations and regional
1004 budgets, 105, 24689–24712, https://doi.org/10.1029/2000JD900385, 2000.

Collins, W. J., Lamarque, J.-F., Schulz, M., Boucher, O., Eyring, V., Hegglin, M. I., Maycock, A., Myhre, G., Prather, M., Shindell, D., and Smith, S. J.: AerChemMIP: quantifying the effects of chemistry and aerosols in CMIP6, 10, 585–607, https://doi.org/10.5194/gmd-10-585-2017, 2017.

Cosme, E., Genthon, C., Martinerie, P., Boucher, O., and Pham, M.: The sulfur cycle at high-southern latitudes in the LMD-ZT General Circulation Model, 107, ACH 7-1-ACH 7-19, https://doi.org/10.1029/2002JD002149, 2002.

Dee, D. P., Uppala, S. M., Simmons, A. J., Berrisford, P., Poli, P., Kobayashi, S., Andrae, U., Balmaseda, M. A., Balsamo, G., Bauer, P., Bechtold, P., Beljaars, A. C. M., van de Berg, L., Bidlot, J., Bormann, N., Delsol, C., Dragani, R., Fuentes, M., Geer, A. J., Haimberger, L., Healy, S. B., Hersbach, H., Hólm, E. V., Isaksen, L., Kållberg, P., Köhler, M., Matricardi, M., McNally, A. P., Monge-Sanz, B. M., Morcrette, J.-J., Park, B.-K., Peubey, C., de Rosnay, P., Tavolato, C., Thépaut, J.-N., and Vitart, F.: The ERA-Interim reanalysis: configuration and performance of the data assimilation system, 137, 553–597, https://doi.org/10.1002/qj.828, 2011.

Faloona, I.: Sulfur processing in the marine atmospheric boundary layer: A review and critical assessment of modeling uncertainties, Atmospheric Environment, 43, 2841–2854, https://doi.org/10.1016/j.atmosenv.2009.02.043, 2009.

Fung, K. M., Heald, C. L., Kroll, J. H., Wang, S., Jo, D. S., Gettelman, A., Lu, Z., Liu, X., Zaveri, R. A., Apel, E., Blake, D. R., Jimenez, J.-L., Campuzano-Jost, P., Veres, P., Bates, T. S., Shilling, J. E., and Zawadowicz, M.: Exploring DMS oxidation and implications for global aerosol radiative forcing, 1–58, https://doi.org/10.5194/acp-2021-782, 2021.

Galí, M., Levasseur, M., Devred, E., Simó, R., and Babin, M.: Sea-surface dimethylsulfide (DMS) concentration from satellite data at global and regional scales, Biogeosciences, 15, 3497–3519, https://doi.org/10.5194/bg-15-3497-2018, 2018.

Glasow, R. von, Sander, R., Bott, A., and Crutzen, P. J.: Modeling halogen chemistry in the marine boundary layer 1. Cloud-free MBL, 107, ACH 9-1-ACH 9-16, https://doi.org/10.1029/2001JD000942, 2002.

Griffiths, P. T., Murray, L. T., Zeng, G., Shin, Y. M., Abraham, N. L., Archibald, A. T., Deushi, M., Emmons, L. K., Galbally, I. E., Hassler, B., Horowitz, L. W., Keeble, J., Liu, J., Moeini, O., Naik, V., O'Connor, F. M., Oshima, N., Tarasick, D., Tilmes, S., Turnock, S. T., Wild, O., Young, P. J., and Zanis, P.: Tropospheric ozone in CMIP6 simulations, Atmos. Chem. Phys., 21, 4187–4218, https://doi.org/10.5194/acp-21-4187-2021, 2021.

Guenther, A. B., Jiang, X., Heald, C. L., Sakulyanontvittaya, T., Duhl, T., Emmons, L. K., and Wang, X.: The Model of Emissions of Gases and Aerosols from Nature version 2.1 (MEGAN2.1): an extended and updated framework for modeling biogenic emissions, 5, 1471–1492, https://doi.org/10.5194/gmd-5-1471-2012, 2012.

Hezel, P. J., Alexander, B., Bitz, C. M., Steig, E. J., Holmes, C. D., Yang, X., and Sciare, J.: Modeled methanesulfonic acid (MSA) deposition in Antarctica and its relationship to sea ice, 116, https://doi.org/10.1029/2011JD016383, 2011.

1034 Ho, S., Peng, L., Anthes, R. A., Kuo, Y.-H., and Lin, H.-C.: Marine Boundary Layer Heights and Their Longitudinal, Diurnal,
1035 and Interseasonal Variability in the Southeastern Pacific Using COSMIC, CALIOP, and Radiosonde Data, J. Climate, 28,
1036 2856–2872, https://doi.org/10.1175/JCLI-D-14-00238.1, 2015.

1037 Hoesly, R. M., Smith, S. J., Feng, L., Klimont, Z., Janssens-Maenhout, G., Pitkanen, T., Seibert, J. J., Vu, L., Andres, R. J.,
1038 Bolt, R. M., Bond, T. C., Dawidowski, L., Kholod, N., Kurokawa, J., Li, M., Liu, L., Lu, Z., Moura, M. C. P., O'Rourke, P.
1039 R., and Zhang, Q.: Historical (1750–2014) anthropogenic emissions of reactive gases and aerosols from the Community
1040 Emissions Data System (CEDS), 11, 369–408, https://doi.org/10.5194/gmd-11-369-2018, 2018.

1041 Hoffmann, E. H., Tilgner, A., Schrödner, R., Bräuer, P., Wolke, R., and Herrmann, H.: An advanced modeling study on the
1042 impacts and atmospheric implications of multiphase dimethyl sulfide chemistry, PNAS, 113, 11776–11781,
1043 https://doi.org/10.1073/pnas.1606320113, 2016.

1044 Hoffmann, E. H., Heinold, B., Kubin, A., Tegen, I., and Herrmann, H.: The Importance of the Representation of DMS
1045 Oxidation in Global Chemistry-Climate Simulations, 48, e2021GL094068, https://doi.org/10.1029/2021GL094068, 2021.

1046 Hulswar, S., Simó, R., Galí, M., Bell, T. G., Lana, A., Inamdar, S., Halloran, P. R., Manville, G., and Mahajan, A. S.: Third
1047 revision of the global surface seawater dimethyl sulfide climatology (DMS-Rev3), Earth Syst. Sci. Data, 14, 2963–2987,
1048 https://doi.org/10.5194/essd-14-2963-2022, 2022.

1049 Jenkin, M. E., Young, J. C., and Rickard, A. R.: The MCM v3.3.1 degradation scheme for isoprene, 15, 11433–11459,
1050 https://doi.org/10.5194/acp-15-11433-2015, 2015.

1051 Jenkin, M. E., Khan, M. A. H., Shallcross, D. E., Bergström, R., Simpson, D., Murphy, K. L. C., and Rickard, A. R.: The CRI
1052 v2.2 reduced degradation scheme for isoprene, Atmospheric Environment, 212, 172–182,
1053 https://doi.org/10.1016/j.atmosenv.2019.05.055, 2019.

1054 Jernigan, C.M., Fite, C.H., Vereecken, L., Berkelhammer, M.B., Rollins, A.W., Rickly, P.S., Novelli, A., Taraborrelli, D.,
1055 Holmes, C.D. and Bertram, T.H. Efficient Production of Carbonyl Sulfide in the Low-NOx Oxidation of Dimethyl Sulfide.
1056 Geophysical Research Letters, 49(3), p.e2021GL096838. 2022.

1057 Karl, M., Gross, A., Leck, C., and Pirjola, L.: Intercomparison of dimethylsulfide oxidation mechanisms for the marine
1058 boundary layer: Gaseous and particulate sulfur constituents, 112, https://doi.org/10.1029/2006JD007914, 2007.

1059 Khan, M. A. H., Gillespie, S. M. P., Razis, B., Xiao, P., Davies-Coleman, M. T., Percival, C. J., Derwent, R. G., Dyke, J. M.,
1060 Ghosh, M. V., Lee, E. P. F., and Shallcross, D. E.: A modelling study of the atmospheric chemistry of DMS using the global
1061 model, STOCHEM-CRI, Atmospheric Environment, 127, 69–79, https://doi.org/10.1016/j.atmosenv.2015.12.028, 2016.

Khan, M. A. H., Bannan, T. J., Holland, R., Shallcross, D. E., Archibald, A. T., Matthews, E., Back, A., Allan, J., Coe, H., Artaxo, P., and Percival, C. J.: Impacts of Hydroperoxymethyl Thioformate on the Global Marine Sulfur Budget, ACS Earth Space Chem., 5, 2577–2586, https://doi.org/10.1021/acsearthspacechem.1c00218, 2021.

Knote, C., Tuccella, P., Curci, G., Emmons, L., Orlando, J. J., Madronich, S., Baró, R., Jiménez-Guerrero, P., Luecken, D., Hogrefe, C., Forkel, R., Werhahn, J., Hirtl, M., Pérez, J. L., San José, R., Giordano, L., Brunner, D., Yahya, K., and Zhang, Y.: Influence of the choice of gas-phase mechanism on predictions of key gaseous pollutants during the AQMEII phase-2 intercomparison, Atmospheric Environment, 115, 553–568, https://doi.org/10.1016/j.atmosenv.2014.11.066, 2015.

Lee, C., Martin, R. V., van Donkelaar, A., Lee, H., Dickerson, R. R., Hains, J. C., Krotkov, N., Richter, A., Vinnikov, K., and Schwab, J. J.: SO2 emissions and lifetimes: Estimates from inverse modeling using in situ and global, space-based (SCIAMACHY and OMI) observations, J. Geophys. Res.-Atmos., 116, D06304, https://doi.org/10.1029/2010JD014758, 2011.

McKee, M. L.: Theoretical study of thet CH3SOO radical, Chemical Physics Letters, 211, 643–648, https://doi.org/10.1016/0009-2614(93)80157-K, 1993.

Minikin, A., Legrand, M., Hall, J., Wagenbach, D., Kleefeld, C., Wolff, E., Pasteur, E. C., and Ducroz, F.: Sulfur-containing species (sulfate and methanesulfonate) in coastal Antarctic aerosol and precipitation, 103, 10975–10990, https://doi.org/10.1029/98JD00249, 1998.

Mulcahy, J.P., Jones, C., Sellar, A., Johnson, B., Boutle, I.A., Jones, A., Andrews, T., Rumbold, S.T., Mollard, J., Bellouin, N. and Johnson, C.E. Improved aerosol processes and effective radiative forcing in HadGEM3 and UKESM1. Journal of Advances in Modeling Earth Systems, 10(11), pp.2786-2805. 2018.

Mulcahy, J. P., Johnson, C., Jones, C. G., Povey, A. C., Scott, C. E., Sellar, A., Turnock, S. T., Woodhouse, M. T., Abraham, N. L., Andrews, M. B., Bellouin, N., Browse, J., Carslaw, K. S., Dalvi, M., Folberth, G. A., Glover, M., Grosvenor, D. P., Hardacre, C., Hill, R., Johnson, B., Jones, A., Kipling, Z., Mann, G., Mollard, J., O'Connor, F. M., Palmiéri, J., Reddington, C., Rumbold, S. T., Richardson, M., Schutgens, N. A. J., Stier, P., Stringer, M., Tang, Y., Walton, J., Woodward, S., and Yool, A.: Description and evaluation of aerosol in UKESM1 and HadGEM3-GC3.1 CMIP6 historical simulations, 13, 6383–6423, https://doi.org/10.5194/gmd-13-6383-2020, 2020.

Novak, G. A., Fite, C. H., Holmes, C. D., Veres, P. R., Neuman, J. A., Faloona, I., Thornton, J. A., Wolfe, G. M., Vermeuel, M. P., Jernigan, C. M., Peischl, J., Ryerson, T. B., Thompson, C. R., Bourgeois, I., Warneke, C., Gkatzelis, G. I., Coggon, M. M., Sekimoto, K., Bui, T. P., Dean-Day, J., Diskin, G. S., DiGangi, J. P., Nowak, J. B., Moore, R. H., Wiggins, E. B., Winstead, E. L., Robinson, C., Thornhill, K. L., Sanchez, K. J., Hall, S. R., Ullmann, K., Dollner, M., Weinzierl, B., Blake, D. R., and Bertram, T. H.: Rapid cloud removal of dimethyl sulfide oxidation products limits SO2 and cloud condensation nuclei production in the marine atmosphere, PNAS, 118, https://doi.org/10.1073/pnas.2110472118, 2021.

Pacifico, F., Harrison, S. P., Jones, C. D., Arneth, A., Sitch, S., Weedon, G. P., Barkley, M. P., Palmer, P. I., Serça, D., Potosnak, M., Fu, T.-M., Goldstein, A., Bai, J., and Schurgers, G.: Evaluation of a photosynthesis-based biogenic isoprene emission scheme in JULES and simulation of isoprene emissions under present-day climate conditions, 11, 4371–4389, https://doi.org/10.5194/acp-11-4371-2011, 2011.

Pham, M., Müller, J.-F., Brasseur, G. P., Granier, C., and Mégie, G.: A three-dimensional study of the tropospheric sulfur cycle, 100, 26061–26092, https://doi.org/10.1029/95JD02095, 1995.

Ranjithkumar, A., Gordon, H., Williamson, C., Rollins, A., Pringle, K., Kupc, A., Abraham, N. L., Brock, C., and Carslaw, K.: Constraints on global aerosol number concentration, SO2 and condensation sink in UKESM1 using ATom measurements, Atmos. Chem. Phys., 21, 4979–5014, https://doi.org/10.5194/acp-21-4979-2021, 2021.

Sander, R.: Compilation of Henry's law constants (version 4.0) for water as solvent, Atmos. Chem. Phys., 15, 4399–4981, https://doi.org/10.5194/acp-15-4399-2015, 2015, corrigendum, 2021.

Sandu, A. and Sander, R.: Technical note: Simulating chemical systems in Fortran90 and Matlab with the Kinetic PreProcessor KPP-2.1, 6, 187–195, https://doi.org/10.5194/acp-6-187-2006, 2006.

Sciare, J., Mihalopoulos, N., and Dentener, F. J.: Interannual variability of atmospheric dimethylsulfide in the southern Indian Ocean, J. Geophys. Res., 105, 26369–26377, https://doi.org/10.1029/2000JD900236, 2000.

Sciare, J., Baboukas, E., and Mihalopoulos, N.: Short-Term Variability of Atmospheric DMS and Its Oxidation Products at Amsterdam Island during Summer Time, Journal of Atmospheric Chemistry, 39, 281–302, https://doi.org/10.1023/A:1010631305307, 2001.

Sellar, A. A., Jones, C. G., Mulcahy, J. P., Tang, Y., Yool, A., Wiltshire, A., O'Connor, F. M., Stringer, M., Hill, R., Palmieri, J., Woodward, S., Mora, L. de, Kuhlbrodt, T., Rumbold, S. T., Kelley, D. I., Ellis, R., Johnson, C. E., Walton, J., Abraham, N. L., Andrews, M. B., Andrews, T., Archibald, A. T., Berthou, S., Burke, E., Blockley, E., Carslaw, K., Dalvi, M., Edwards, J., Folberth, G. A., Gedney, N., Griffiths, P. T., Harper, A. B., Hendry, M. A., Hewitt, A. J., Johnson, B., Jones, A., Jones, C. D., Keeble, J., Liddicoat, S., Morgenstern, O., Parker, R. J., Predoi, V., Robertson, E., Siahaan, A., Smith, R. S., Swaminathan, R., Woodhouse, M. T., Zeng, G., and Zerroukat, M.: UKESM1: Description and Evaluation of the U.K. Earth System Model, 11, 4513–4558, https://doi.org/10.1029/2019MS001739, 2019.

Sellar, A. A., Walton, J., Jones, C. G., Wood, R., Abraham, N. L., Andrejczuk, M., Andrews, M. B., Andrews, T., Archibald, A. T., de Mora, L., Dyson, H., Elkington, M., Ellis, R., Florek, P., Good, P., Gohar, L., Haddad, S., Hardiman, S. C., Hogan, E., Iwi, A., Jones, C. D., Johnson, B., Kelley, D. I., Kettleborough, J., Knight, J. R., Köhler, M. O., Kuhlbrodt, T., Liddicoat, S., Linova-Pavlova, I., Mizielinski, M. S., Morgenstern, O., Mulcahy, J., Neininger, E., O'Connor, F. M., Petrie, R., Ridley, J., Rioual, J.-C., Roberts, M., Robertson, E., Rumbold, S., Seddon, J., Shepherd, H., Shim, S., Stephens, A., Teixiera, J. C., Tang, Y., Williams, J., Wiltshire, A., and Griffiths, P. T.: Implementation of U.K. Earth System Models for CMIP6, 12, e2019MS001946, https://doi.org/10.1029/2019MS001946, 2020.

Stevenson, D. S., Zhao, A., Naik, V., O'Connor, F. M., Tilmes, S., Zeng, G., Murray, L. T., Collins, W. J., Griffiths, P. T., Shim, S., Horowitz, L. W., Sentman, L. T., and Emmons, L.: Trends in global tropospheric hydroxyl radical and methane lifetime since 1850 from AerChemMIP, Atmos. Chem. Phys., 20, 12905–12920, https://doi.org/10.5194/acp-20-12905-2020, 2020.

Sutton, R.T., McCarthy, G.D., Robson, J., Sinha, B., Archibald, A.T. and Gray, L.J. Atlantic multidecadal variability and the UK ACSIS program. Bulletin of the American Meteorological Society, 99(2), pp.415-425. 2018.

Telford, P. J., Abraham, N. L., Archibald, A. T., Braesicke, P., Dalvi, M., Morgenstern, O., O'Connor, F. M., Richards, N. a. D., and Pyle, J. A.: Implementation of the Fast-JX Photolysis scheme (v6.4) into the UKCA component of the MetUM chemistry-climate model (v7.3), 6, 161–177, https://doi.org/10.5194/gmd-6-161-2013, 2013.

Tesdal, J.-E., Christian, J. R., Monahan, A. H., Salzen, K. von, Tesdal, J.-E., Christian, J. R., Monahan, A. H., and Salzen, K. von: Evaluation of diverse approaches for estimating sea-surface DMS concentration and air–sea exchange at global scale, Environ. Chem., 13, 390–412, https://doi.org/10.1071/EN14255, 2015.

Thomas, E.R., Allen, C.S., Etourneau, J., King, A.C., Severi, M., Winton, V.H.L., Mueller, J., Crosta, X. and Peck, V.L. Antarctic sea ice proxies from marine and ice core archives suitable for reconstructing sea ice over the past 2000 years. Geosciences, 9(12), 506. 2019.

Turnipseed, A. A., Barone, S. B., and Ravishankara, A. R.: Observation of methylthiyl radical addition to oxygen in the gas phase, J. Phys. Chem., 96, 7502–7505, https://doi.org/10.1021/j100198a006, 1992.

Urbanski, S. P., Stickel, R. E., and Wine, P. H.: Mechanistic and Kinetic Study of the Gas-Phase Reaction of Hydroxyl Radical with Dimethyl Sulfoxide, J. Phys. Chem. A, 102, 10522–10529, https://doi.org/10.1021/jp9833911, 1998.

Veres, P. R., Neuman, J. A., Bertram, T. H., Assaf, E., Wolfe, G. M., Williamson, C. J., Weinzierl, B., Tilmes, S., Thompson, C. R., Thames, A. B., Schroder, J. C., Saiz-Lopez, A., Rollins, A. W., Roberts, J. M., Price, D., Peischl, J., Nault, B. A., Møller, K. H., Miller, D. O., Meinardi, S., Li, Q., Lamarque, J.-F., Kupc, A., Kjaergaard, H. G., Kinnison, D., Jimenez, J. L., Jernigan, C. M., Hornbrook, R. S., Hills, A., Dollner, M., Day, D. A., Cuevas, C. A., Campuzano-Jost, P., Burkholder, J., Bui, T. P., Brune, W. H., Brown, S. S., Brock, C. A., Bourgeois, I., Blake, D. R., Apel, E. C., and Ryerson, T. B.: Global airborne sampling reveals a previously unobserved dimethyl sulfide oxidation mechanism in the marine atmosphere, Proc Natl Acad Sci USA, 117, 4505–4510, https://doi.org/10.1073/pnas.1919344117, 2020.

Vermeuel, M. P., Novak, G. A., Jernigan, C. M., and Bertram, T. H.: Diel Profile of Hydroperoxymethyl Thioformate: Evidence for Surface Deposition and Multiphase Chemistry, Environ. Sci. Technol., 54, 12521–12529, https://doi.org/10.1021/acs.est.0c04323, 2020.

von Glasow, R. and Crutzen, P. J.: Model study of multiphase DMS oxidation with a focus on halogens, Atmos. Chem. Phys., 4, 589–608, https://doi.org/10.5194/acp-4-589-2004, 2004.

Walters, D., Baran, A. J., Boutle, I., Brooks, M., Earnshaw, P., Edwards, J., Furtado, K., Hill, P., Lock, A., Manners, J., Morcrette, C., Mulcahy, J., Sanchez, C., Smith, C., Stratton, R., Tennant, W., Tomassini, L., Van Weverberg, K., Vosper, S., Willett, M., Browse, J., Bushell, A., Carslaw, K., Dalvi, M., Essery, R., Gedney, N., Hardiman, S., Johnson, B., Johnson, C., Jones, A., Jones, C., Mann, G., Milton, S., Rumbold, H., Sellar, A., Ujiie, M., Whitall, M., Williams, K., and Zerroukat, M.: The Met Office Unified Model Global Atmosphere 7.0/7.1 and JULES Global Land 7.0 configurations, 12, 1909–1963, https://doi.org/10.5194/gmd-12-1909-2019, 2019.

Wang, X., Jacob, D. J., Downs, W., Zhai, S., Zhu, L., Shah, V., Holmes, C. D., Sherwen, T., Alexander, B., Evans, M. J., Eastham, S. D., Neuman, J. A., Veres, P. R., Koenig, T. K., Volkamer, R., Huey, L. G., Bannan, T. J., Percival, C. J., Lee, B. H., and Thornton, J. A.: Global tropospheric halogen (Cl, Br, I) chemistry and its impact on oxidants, 21, 13973–13996, https://doi.org/10.5194/acp-21-13973-2021, 2021.

Weber, J., Archer-Nicholls, S., Griffiths, P., Berndt, T., Jenkin, M., Gordon, H., Knote, C., and Archibald, A. T.: CRI-HOM: A novel chemical mechanism for simulating highly oxygenated organic molecules (HOMs) in global chemistry–aerosol–climate models, Atmos. Chem. Phys., 20, 10889–10910, https://doi.org/10.5194/acp-20-10889-2020, 2020.

Weber, J., Archer-Nicholls, S., Abraham, N. L., Shin, Y. M., Bannan, T. J., Percival, C. J., Bacak, A., Artaxo, P., Jenkin, M., Khan, M. A. H., Shallcross, D. E., Schwantes, R. H., Williams, J., and Archibald, A. T.: Improvements to the representation of BVOC chemistry–climate interactions in UKCA (v11.5) with the CRI-Strat 2 mechanism: incorporation and evaluation, 14, 5239–5268, https://doi.org/10.5194/gmd-14-5239-2021, 2021.

Wells, K.C., Millet, D.B., Payne, V.H., Deventer, M.J., Bates, K.H., de Gouw, J.A., Graus, M., Warneke, C., Wisthaler, A. and Fuentes, J.D. Satellite isoprene retrievals constrain emissions and atmospheric oxidation. Nature, 585(7824), 225-233. 2020.

Wennberg, P. O., Bates, K. H., Crounse, J. D., Dodson, L. G., McVay, R. C., Mertens, L. A., Nguyen, T. B., Praske, E., Schwantes, R. H., Smarte, M. D., St Clair, J. M., Teng, A. P., Zhang, X., and Seinfeld, J. H.: Gas-Phase reactions of isoprene and its major oxidation products, Chem. Rev., 118, 3337–3390, https://doi.org/10.1021/acs.chemrev.7b00439, 2018.

Wofsy, S. C., Afshar, S., Allen, H. M., Apel, E. C., Asher, E. C., Barletta, B., Bent, J., Bian, H., Biggs, B. C., Blake, D. R., Blake, N., Bourgeois, I., Brock, C. A., Brune, W. H., Budney, J. W., Bui, T. P., Butler, A., Campuzano-Jost, P., Chang, C. S., Chin, M., Commane, R., Corr, G., and Zeng, L. H.: ATom: merged atmospheric chemistry, trace gases, and aerosols, data set, ORNL DAAC, Oak Ridge, Tennessee, USA, https://doi.org/10.3334/ORNLDAAC/1581, 2018.

Wollesen de Jonge, R., Elm, J., Rosati, B., Christiansen, S., Hyttinen, N., Lüdemann, D., Bilde, M., and Roldin, P.: Secondary aerosol formation from dimethyl sulfide – improved mechanistic understanding based on smog chamber experiments and modelling, 21, 9955–9976, https://doi.org/10.5194/acp-21-9955-2021, 2021.

1186 Wu, R., Wang, S., and Wang, L.: New Mechanism for the Atmospheric Oxidation of Dimethyl Sulfide. The Importance of
1187 Intramolecular Hydrogen Shift in a CH$_3$SCH$_2$OO Radical, J. Phys. Chem. A, 119, 112–117, https://doi.org/10.1021/jp511616j,
1188 2015.

1189 Ye, Q., Goss, M. B., Isaacman-VanWertz, G., Zaytsev, A., Massoli, P., Lim, C., Croteau, P., Canagaratna, M., Knopf, D. A.,
1190 Keutsch, F. N., Heald, C. L., and Kroll, J. H.: Organic Sulfur Products and Peroxy Radical Isomerization in the OH Oxidation
1191 of Dimethyl Sulfide, ACS Earth Space Chem., https://doi.org/10.1021/acsearthspacechem.1c00108, 2021.
1192